Combustion and Flame 269 (2024) 113703

Contents lists available at ScienceDirect

Combustion and Flame

journal homepage: www.sciencedirect.com/journal/combustion-and-flame

Role of volatile secondary char on the combustion behavior of cellulose-based hydrochars

Parvaneh Motiei [a], Matteo Pecchi [b], James L. Adair [b], Jillian L. Goldfarb [b,c], Jacqueline O'Connor [a,*]

[a] Mechanical Engineering, Pennsylvania State University, University Park, PA USA
[b] Biological and Environmental Engineering, Cornell University, Ithaca, NY USA
[c] Smith School of Chemical and Biomolecular Engineering, Cornell University, Ithaca, NY USA

ARTICLE INFO

Keywords:
Hydrochar
Hydrothermal carbonization
Ignition
Devolatilization
Biofuel combustion
Secondary char

ABSTRACT

Hydrothermal carbonization (HTC) can transform a wide range of biomass into renewable biofuels. Hydrochar, the solid fuel resulting from HTC, has a similar energy density to low-rank coals. Despite an extensive body of literature detailing the thermogravimetric analysis (TGA) of hydrochar under slow pyrolysis and oxidation, there remains a limited understanding of hydrochar's behavior in realistic combustion settings. In this work, we integrate combustion experiments and TGA to understand the combustion characteristics of a model hydrochar fuel. Cellulose-based hydrochars produced at different temperatures along with solvent-extracted chars are tested in a Hencken burner across varying temperatures and oxygen concentrations in the oxidizer gas. Simultaneous CH* chemiluminescence, particle image velocimetry, and two-color pyrometry are used to measure ignition delay time and identify homogeneous/heterogeneous ignition mechanisms and combustion phases. Incorporating TGA with combustion results shows that the ignition mode and combustion processes are strong functions of surrounding gas temperature and oxygen mole fraction. The level of carbonization of the hydrochar dictates the ignition delay time and combustion modes. Further, the presence of a tar-like secondary char on the as-carbonized hydrochars leads to more rapid ignition due to high volatility.

1. Introduction

World-wide decarbonization pledges are driving a shift towards renewable biomass-based fuels for clean power generation and industrial processes [1]. Hydrothermal carbonization (HTC) is a promising method to upgrade wet residual biomass into energy-dense carbonaceous hydrochar (HC) by treating the biomass in a subcritical aqueous environment under high pressure and temperature [2]. Despite its widely touted use as a solid fuel, little is known about the fundamental combustion characteristics of HCs. While the fuel scientists that produce these fuels often discuss their combustibility, such statements are usually supported only by higher heating value measurements and slow heating rate thermogravimetric analyses (TGA). This study is one of the first to explore ignition delay time and combustion modes of HCs using a Hencken burner with several simultaneous diagnostics. The combustion experiments are analyzed alongside TGA data to develop unique cross-disciplinary methods to quantify the combustion performance of these renewable solid fuels.

Depending on HTC process conditions, the resulting HCs can resemble a lignite or even high-volatile bituminous coal [3]. Typically, HC has a higher fixed carbon content, higher energy density, higher ignition temperature, more stable flame, and lower ash content than unprocessed biomass. As such, HC has fewer and less severe potential self-ignition hazards than raw biomass [4,5]. These beneficial properties are a result of the biomass being transformed via deoxygenation, dehydration, and decarboxylation reactions that intensify with severity, which is defined as the residence time in and temperature of the reactor [6]. HC forms via two pathways: (1) solid-solid conversion, in which the HC maintains some structure and morphology of the parent biomass – this phase is referred to as primary char (PC); and (2) degradation of the biomass into the aqueous phase followed by partial polymerization of organic molecules back onto the solid phase [7] – this phase is called secondary char (SC). SC is often identified as amorphous microspheres on the surface of the PC and is comprised mainly of volatile and semi-volatile organic compounds [8]. SC can be recovered using thermal or solvent extraction and thus its yield varies depending on the composition and extraction method. For solvent extraction, yield is

---

* Corresponding author.
E-mail address: jxo22@psu.edu (J. O'Connor).

https://doi.org/10.1016/j.combustflame.2024.113703
Received 12 May 2024; Received in revised form 26 August 2024; Accepted 27 August 2024

Nomenclature

CLS	Raw cellulos
DTG	Derivative thermogravimetry
FC	Fixed carbon
HC	Hydrochar
HC220	As-carbonized hydrochar synthesized from cellulose by HTC at 220°C
HC250	As-carbonized hydrochar synthesized from cellulose by HTC at 250°C
HHV	Higher heating value [MJ/kg]
HTC	Hydrothermal carbonization
PC	Primary char
PC220	Primary char produced from solvent extraction of HC220
PC250	Primary char produced from solvent extraction of HC250
SC	Secondary char
T_{ad}	Adiabatic flame temperature [K]
TGA	Thermogravimetric analysis
VM	Volatile matter
u	Velocity [m/s]
x	Downstream distance [m]
τ_{ig}	Ignition delay time [sec]

quantified as the mass fraction of the HC that can be dissolved (or suspended) into organic solvents [9]; while polar and non-polar solvents maximize the extraction of polar and non-polar compounds in the SC, respectively [10]. Both feedstock and, particularly, reaction temperature influence HC properties and the yield and composition of SC [5,11, 12,9,13–16]. For example, increasing the HTC temperature and residence time increases the fixed carbon content as the biomass' volatiles are partitioned into the aqueous phase. However, TGA studies show that while higher HTC temperatures produce HC with more fixed carbon, such HCs also exhibit higher thermal reactivity. This property is attributed to the volatile SC deposited on the HC during HTC. Solvent washing (extraction) HCs can remove the volatile SC to produce a solid material (PC) that more closely mimics coal behavior [3,17]. Besides shifting PC properties towards those of a coal, solvent extraction enables the recovery of SC, a liquid fuel precursor [18,19].

Despite the growing popularity of HTC, there are limited studies on direct combustion of HC, considered as a renewable biofuel [20–24], and none, to the authors' knowledge, that investigate the impact of SC on HC combustion. However, a substantial body of literature exists on pulverized carbonaceous solid fuel and raw biomass combustion, exploring the effects of particle size, fuel rank, oxidizing atmosphere, diluent agent, and surrounding gas temperature on combustion timescales, ignition temperature, and ignition modes [25–33]. The results of these studies inform the interpretation of the combustion experiments of HCs. In general, combustion experiments of solid fuels showed that higher co-flow temperature and O_2 concentration result in lower ignition delay time, volatile burnout time, char burnout time, and ignition temperature [25–33]. In the present study, we vary fuel carbonization level, O_2 mole fraction, and surrounding gas temperature to understand the impact on combustion behaviors of HCs and PCs.

In general, there are three different modes of particle ignition: homogeneous ignition, where ignition first occurs in the gaseous volatiles released from the solid fuel; heterogeneous ignition, where ignition first occurs on the surface of the solid fuel; and a mixed ignition mode, where both solid- and volatile-phase ignition occurs simultaneously. The ignition mechanism depends on both the flammability limit of the released volatiles and the relative timescales of particle surface heating to volatile release [28,34–36]. Several studies have been carried out to determine the ignition mechanism of both isolated particles [31,37–41] and a stream of particles [28,35,36]. Ambient temperature, O_2 concentration, volatile matter, and particle size are the major parameters that affect reaction kinetics and thus determine the ignition mechanism of solid fuel particles. Coal particles typically ignite homogeneously under high temperature and low O_2 concentration for larger particles, and they ignite heterogeneously at low temperatures and high O_2 concentration for smaller particles. The earlier release of volatiles with higher ambient temperature limits O_2 diffusion to the surface due to the formation of a volatile layer and leads to homogeneous ignition of gaseous volatiles. Homogeneous ignition is more likely to occur for lower rank solid fuels, which contain more volatile matter[28,35,42].

In this work, experimental combustion studies are combined with TGA to provide a deeper understanding of the ignition mechanism of HC and PC under various oxidizing conditions. TGA is routinely used by (bio)fuel scientists to study pyrolysis and slow oxidation of solid fuels; the renewable fuel literature is replete with TGA of HC [43–51]. These works collectively demonstrate TGA as a valuable tool for assessing the proximate content (volatile matter, fixed carbon, ash) of solid biofuels. They further show that derivative thermogravimetric analysis (DTG) can be used to determine the peak temperatures and reaction rates as solid fuels devolatilize or oxidize. Despite the vast majority of papers in the fuel science literature assessing HC "combustion" behavior via TGA [52–54], there is little evidence that TGA alone can conclusively assess of the suitability of a material as a fuel in true combustion environment. The major limitation of TGA is its inability to realistically mimic real combustion conditions because the TGA heating rates (0.1–100 K/min) are orders of magnitude slower compared to rapid heating conditions in real combustors ($\sim 10^5$ K/s) [55]. Studies report conflicting trends when relating oxidation reactivity under slow TGA heating rates to rapid heating conditions in real combustion processes [56–58]. Conflicting results are attributed to the transport process being primarily kinetically-controlled in TGA versus being diffusion-controlled in combustors [59–61]. Under the slower heating rates of TGA, particles may devolatilize more slowly; many TGA studies demonstrate the dependence of pyrolysis reaction rates on heating rate [62]. Further, TGA lacks the fluid-dynamic interactions that are important in combustion scenarios, including particle-to-particle interactions and fluid-chemical coupling, such that extrapolation of reactivity parameters found from TGA to combustion scenarios is difficult. Hence, it is useful to assess HC combustion behavior under rapid oxidative environment alongside TGA to develop deeper insight into its fundamental combustion characterization, which is one of the major goals of the present work.

In this paper, we discuss the impacts of co-flow temperature, O_2 mole fraction, fuel rank, as well as the intervening role of SC on ignition delay time, ignition mode, and combustion behaviors of cellulose-derived HCs. Previous work from the literature suggests that the SC could have an important effect on the ignition of these materials due to its higher volatility and chemically reactive composition. Further, it has been well established in the solid fuel literature that fuel rank has a significant effect on both ignition and burnout processes, but this dependency has not been studied for materials synthesized using HTC. As such, the goal of this work is to provide an understanding of the fundamental ignition and combustion modes that govern the combustion of these promising fuels. The interpretation of combustion data is supported through the use of TGA and DTG analysis, which provide detailed information about the thermal stability and oxidation processes of these materials.

2. Materials and methods

2.1. Synthesis, extraction, and characterization of HCs

HCs were synthesized from cellulose, chosen as it is a well-characterized model biomass whose HCs have also been well-characterized using TGA [63,64]. Microcrystalline cellulose, sourced from Alfa Aesar, was hydrothermally carbonized at two temperatures, 220°C (HC220) and 250°C (HC250), using the HTC procedure outlined in our prior work [19]. Briefly, cellulose (15% biomass/water ratio) was held at 220°C or 250°C for 1 h in a 1 L stirred stainless steel reactor (Parr Instrument Company, 60% filled volume, initially pressurized under 5-6 bar N_2), before quenching with ice and water to 70°C, upon which the reaction was considered complete. HC yield percentage showed high reproducibility between tests (standard deviation <1%). Manual solvent extraction of HC220 and HC250 was used to separate SC from PC samples (PC220 and PC250, respectively). In triplicate, 0.9 g HC was submerged in 30 mL ethanol (ACS grade, ThermoScientific) in glass scintillation vials and shaken at 150 rpm for 3 h. The SC, now dissolved in the solvent, was recovered by vacuum filtration, leaving solid PC. Individual PC yields following extraction were generally within 5% of the mean PC yield.

Both as-carbonized HC and extracted PC, shown in Fig. 1, were ground and wet sieved to a 25-37 μm fraction. Particle size distributions are measured using a Microtrac particle size analyzer, results of which are shown in the supplementary material. Different levels of carbonization of both HCs are evident from the color differences of materials. While HC220 was medium brown, HC250 was nearly black. HC250 had a slightly oily texture, which became drier and more powder-like after SC extraction. The extraction had negligible effects on color; HCs looked visually similar to their PC counterparts, particularly for the 250°C sample.

2.2. Physicochemical analysis of HC, PC, and SC

Proximate analysis, oxidation behavior, and solid distillation curves were obtained using a TGA 650 Thermogravimetric Analyzer (TA Instruments). Proximate analysis and oxidation reaction curves were performed according to our prior work [63]. For proximate analysis, the sample was heated under an N_2 atmosphere at 383 K until a constant mass was achieved to remove residual moisture, then heated to 1173 K and held to quantify volatile matter released, and then heated to 1223 K under air to oxidize the fixed carbon, leaving ash. For oxidation studies, the atmosphere used was air. After drying the sample at 383 K, the temperature was ramped at three rates (10 K/min, 50 K/min, and 100 K/min) to 1123 K and held until constant mass was obtained. Solid distillation began with a ramp to 383 K at 10 K/min under 25 mL/min N_2, where it was held for 30 min. The temperature was then ramped at 100 K/min to 473 K, held for 30 min; this ramp and hold procedure was repeated at 573, 673, 773, and 873 K. After that, the flow gas switched to air and the temperature was ramped at 50 K/min to 1223 K, held for 30 min to leave ash, and data collection ended. Details of the temperature ramp for the distillation curves are plotted with the data. All thermogravimetric data analysis was performed using an in-house open-source Python package “tga-data-analysis” v2.2.0, available online [65].

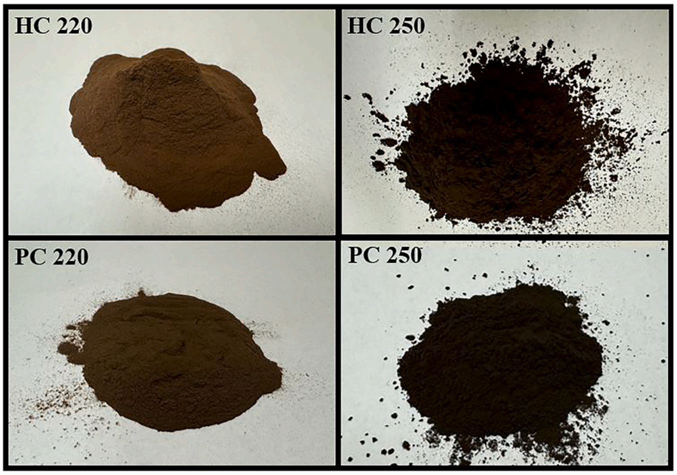

Fig. 1. Images of ground and sieved hydrochar samples.

Elemental (C, H, N, O) analysis of cellulose, HCs, and PCs was performed using a CE-440 Elemental Analyzer (Exeter Analytical) equipped with an autosampler. The calibration was performed using Sulphanilamide samples, as per the manufacturer instructions. Samples were triplicated.

SC was analyzed using a Shimadzu GC 2010 Plus Gas Chromatograph-Mass Spectrometer with a Restek Rtx-5Sil MS 30 m fused silica column. The ethanol containing the SC was dried under vacuum, then reconstituted with dichloromethane. The GC-MS method entailed five pre-run solvent rinses of the injector needle, three with sample, and five post-run. The ion source temperature was 230°C, interface temperature was 320°C, and injection temperature was 280°C. Column oven temperature started at 40°C, ramped to 300°C at 5°C/min, held for 5 min, then ramped to 250°C at -20°C/min, where data collection stopped. Solvent cut time was 6 min and event time (scan period) was 0.4 s. Identified compounds were quantified using an in-house calibration of 88 standard biofuel compounds. Compounds not within our calibration were quantified using the closest calibrated compound by Tanimoto similarity (min = 0.4), a metric used in chem-informatics that compares compounds based on functional group composition. The open-source Python package used in the analysis is named “gcms-data-analysis” and is available online [66].

2.3. Combustion experiments

The combustion experiments were performed in a laminar, optically accessible Hencken burner (Fig. 2(a)), as was done in our previous study [63]. As such, only a brief overview of the experiment, diagnostics, and data analysis methods are provided here. H_2 (2.65-3.72 slpm) and various O_2/N_2 (O_2: 2.51-5.07 slpm and N_2:11.81-15.09 slpm) mixtures served as fuel and oxidizer for the co-flow diffusion flame. Fuel particles were seeded through the fluidized bed using N_2 as the carrier gas with flow rate of 0.38 slpm.

Fig. 2(b) shows an overhead schematic of optical diagnostics. A combination of CH* chemiluminescence imaging and particle image velocimetry (PIV) were used to measure ignition delay time. A flame streak of burning particles was formed once the solid fuels particles entered the post-combustion zone of the H_2 flame. CH* chemiluminescence images of the flame streak indicate the spatial extent of combustion. CH* emission was detected using a PI-MAX (Gen II) camera coupled with a 50 mm f /1.4 lens (Nikon AF NIKKOR) and a 430 nm bandpass optical filter (Andover Corporation, Bandpass Filter, FWHM 10.0 nm). Camera gain and exposure time varied depending on the flame brightness at each operating condition to obtain an acceptable signal-to-noise ratio (~30) and avoid pixel saturation. To allow for comparison, the images were all corrected to the same intensity levels before analysis. At each condition, 100 images with a spatial extend of 240 mm × 240 mm are obtained. More details of the CH* imaging and image processing are provided in the supplementary material and our previous work [63].

To measure the ignition delay time, the results from the CH* imaging were combined with velocity fields collected from high-speed PIV, as in our previous work [63]. The PIV system consisted of a dual-cavity, diode-pumped, solid-state laser (Nd:YAG, Quantronix Hawk Duo-60-M/Rev.A at 532 nm) and a high-speed CMOS camera (Photron FASTCAM SA1.1) filtered with a 60 mm f/2.8 lens (Nikon AF Macro Nikkor). 5000 image pairs were acquired at 2.5 kHz and 1024 × 1024 pixel resolution with an interpulse separation of 36 μs. The masked measurement domain spanned 120 mm × 36 mm. The velocity field was calculated using a multi-pass cross-correlation algorithm (LaVision DaVis 8.3) with interrogation domain sizes from 64 × 64 to 16 × 16 pixels; for each pass, a 50% overlap was used, resulting in a vector spacing of 1.17 mm/vector. The estimated uncertainty of the

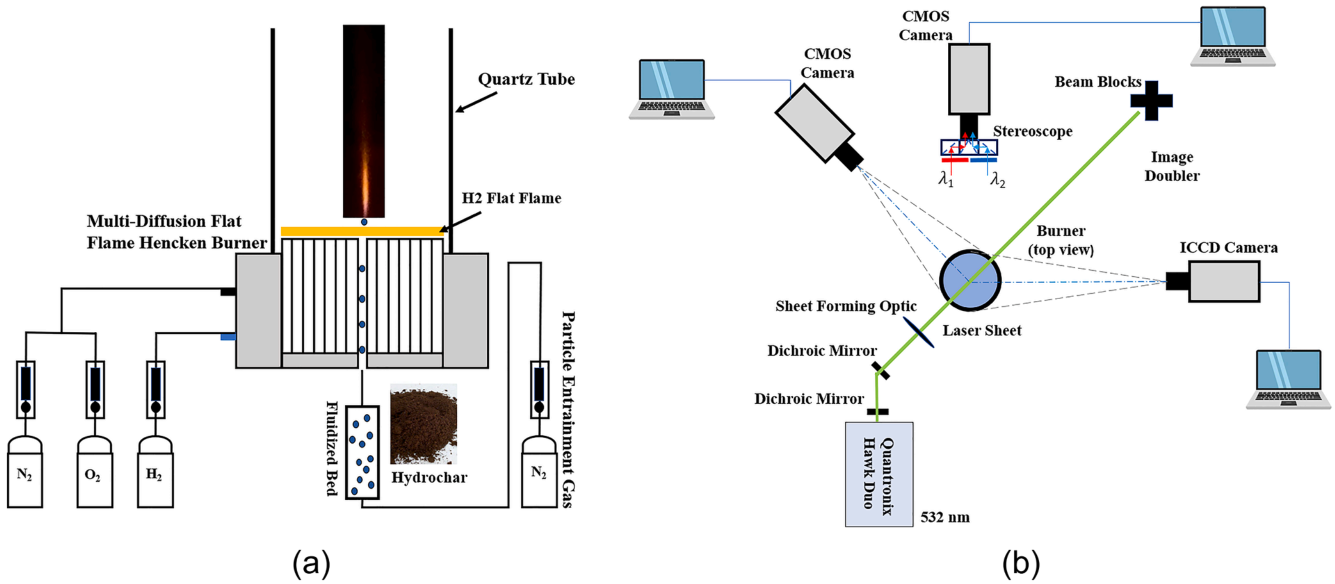

Fig. 2. (a) Schematic of combustion experiment, (b) an overhead schematic of simultaneous optical diagnostics.

time-averaged velocity field based on the correlation statistics in DaVis was 0.01-0.06 m/s in the jet core.

Ignition delay time, τ_{ig}, is calculated as in Eq. (1), where x is downstream distance, x_1 represents the ignition location, and u is time-averaged velocity. Ignition locations are determined based on the maximum gradient intensity criterion of the CH* signal. The details of this methodology, repeatability of measured data, as well as the uncertainty analysis are explained in detail in the supplementary material and in previous work [63].

$$\tau_{ig} = \sum_{i=1}^{i=x_1} \frac{x_{i+1} - x_i}{u_i} \tag{1}$$

Along with CH* chemiluminescence and PIV, a two-color pyrometry technique was used to identify the dominant ignition mode and identify regions where the solid particles were burning. The two-color technique measures the emitted radiation from the burning particles through two channels filtered in different wavelength bands [67]. The incandescence signal strength detected over these two separate spectral regions was a function of the temperature of the solid. By contrast, the CH* imaging measured signal from combustion of both gas-phase and solid-phase reactions. By using the CH* and two-color methods together, we can identify the regions where the solid is burning as regions with high two-color and CH* intensity. Regions with high CH* intensity but no two-color signal are indicative of gas-phase reactions.

The two-color pyrometry setup consisted of a high-speed CMOS sensor camera (Photron FASTCAM SA4) equipped with a 50 mm f/1.4 lens (Nikon AF Nikkor) and a stereoscope with two optical band-pass filters at 680 nm and 800 nm. The stereoscope contains three 30 mm optics cages. The outer two side cages hold two identical dielectric 45° mirrors with the filters affixed to the front facing the burner. A leg-coated right-angle dielectric prism (MRA20L-E02, THORLABS) is embedded in the center cage. The emitted radiation coming from the heated particles passes through the two different filters and is reflected by the mirrors toward the prism. From there, the light beams are turned by the prism onto the camera sensor, creating two images of the particles at two different wavelength bands. An example of time-averaged images of the particles using this technique as well as a discussion of the repeatability of the measurements are provided in the supplementary material. In this study, the two-color technique is not quantitative, but instead used to determine the region of space where the solid phase of the fuel particles was burning. The combination of CH* chemiluminescence imaging and two-color pyrometry can reveal the dominant ignition mode and distinguish between combustion modes [68,25,35]. CH* chemiluminescence emission, produced through the reaction of hydrocarbons with an oxidizing atmosphere, arises from both heterogeneous and homogeneous reactions. The pyrometric signal from the two-color technique is present when heterogeneous reactions heat the particle enough to be detected in the wavelengths used for the techniques. As such, locations where both CH* and pyrometric signals are present are indicative of heterogeneous combustion and locations where CH* signal is strong but no pyrometric signal is present are indicative of homogeneous combustion. Finally, using the two-color imaging to determine particle temperature requires knowledge of the particle emissivity as a function of wavelength and temperature, which was not possible to obtain for this study. As is shown in Fig. 1, the colors of the particles are very different depending on the HTC conditions and also very different from coal, and so no assumptions were made about emissivity.

3. Results and discussion

3.1. Analysis of HTC product phases

HC was carbonized at 220°C and 250°C. At 220°C, 80% of the feedstock remains in the solid phase (Table 1) as hydrochar. At 250°C, the hydrochar yield was 50 wt% (feedstock basis), with the residual mass primarily partitioned into the liquid phase. These results are consistent with previous studies, as higher temperatures affect greater conversion to liquid and gas and 250°C is around the transition point from HTC to hydrothermal liquefaction (HTL) [17].

Although HC yields decreased with temperature, HHV increased with temperature from 220°C to 250°C in HC ($p < 0.0001$, unpaired t-

Table 1
Triplicate HTC yield results for HC, liquid, gas, PC and SC yields for the two investigated temperatures and HC and PC HHV, ± 1 standard deviation. Yields are all on a dry feedstock basis.

Sample	HTC Temp [°C]	Solid Yield [wt%]	Liquid Yield [wt%]	Gas Yield [wt%]	Solid HHV [MJ/kg]
HC220	220	80.3 ± 0.9	19.0 ± 1.0	0.7 ± 0.2	17.9 ± 0.1
PC220	220	58.8 ± 1.1	21.5 ± 1.1		19.3 ± 0.4
HC250	250	49.8 ± 0.7	45.4 ± 0.8	4.8 ± 0.2	27.9 ± 0.3
PC250	250	36.9 ± 1.8	12.9 ± 1.8		31.3 ± 2.4

test) and PC ($p < 0.001$) samples (Table 1). For reference, the HHV of raw cellulose is 17.2 MJ/kg [43], and the increase in HHV for HC250 as compared to the feedstock was 62 %, compared to the 4 % increase seen after HTC at 220°C. The increased severity of HTC at 250°C enhances deoxygenation through decarboxylation and dehydration [69] and as oxygen increases a sample's mass without greatly shifting its total heating value, its removal increases HHV. Extraction of SC resulted in a significant increase in HHV for the 220°C samples ($p < 0.005$, HC220 against PC220), with no statistically significant change for the 250°C samples ($p > 0.01$, HC250 against PC250).

The proximate analysis in Fig. 3(a) shows that HC220 and PC220 have slightly more fixed carbon than raw CLS, while the van Krevelen diagram (Fig. 3(b)) shows slight dehydrogenation and similar O/C ratios. By contrast, HC250 and PC250 have higher fixed carbon and elemental properties comparable to a bituminous coal, with a greater O/C but lower H/C ratio [70,71].

In contrast to HTC temperature, the effect of solvent extraction on VM content was small. Notably, solvent extraction had opposite effects between the two sample types. For HC250, extraction significantly increased the fixed carbon content as it removed volatile matter (unpaired t-test, $p < 0.0001$), while for HC220, this difference was smaller (and insignificant, $p > 0.1$). As less carbonization occurs at 220°C, the solid PC structure remains close to the linked glucose rings that make up the original cellulose. Compositional analysis of the secondary char, shown in detail in the supplementary material, explains these trends. The only detectable compound in the 220°C SC was 5-hydroxymethylfurfural ($C_6H_6O_3$), a compound formed via the dehydration of sugars with an O/C ratio of 0.5 and H/C ratio of 1. Therefore, its removal increases the O/C ratio and decreases H/C ratio (Fig. 3). The primary component of 250°C SC was levulinic acid ($C_5H_8O_3$), with a higher O/C ratio of 0.6. However, a decrease in oxygen in the sample during this extraction was not observed likely due to the other long-chain fatty acids (LCFA) present in the SC (C_{18}, C_{16}, C_{15}). However, as levulinic acid's H/C ratio was 1.6 and the LCFAs H/C were approximately 2, dehydrogenation was observed. In sum, extraction of HC220 had minor effect, while extraction of HC250 increased carbon fraction.

3.2. Effects of variations in gas temperature on ignition mode of HC

Co-flow gas temperature and O_2 mole fraction impact HC combustion processes to varying degrees. Temperature affects both devolatilization and gas-phase kinetic rates, while O_2 mole fraction largely affects reaction kinetics in both the gas and solid phases [63]. In the present work, combustion behavior of HCs is assessed with the test matrix shown Table 2, where gas temperature and O_2 mole fraction are controlled separately.

To determine these conditions, a thermochemical equilibrium calculation for H_2 and a broad range of O_2/N_2 mixtures (O_2 mole fractions of 0.1 – 0.9) with an equivalence ratio range of 0.05-1 was performed in Chemkin-Pro using the GRIMech 3.0 mechanism [72] to determine the adiabatic flame temperature and O_2 mole fraction in the combustion products. The resulting conditions were limited by the operability limits of the Hencken burner but provide a broad range of temperatures and oxygen mole fractions at which to test the combustion processes of the HCs. All conditions were calculated such that the total mass flow of the co-flow and particles are constant, resulting in an exit gas velocity of 0.32 m/s.

First, the results of the experiments at constant oxygen mole fraction and varying temperature are considered. Fig. 4 shows the centerline intensity curves of the flame streak extracted from time-averaged CH* images along the downstream direction for HC220 for temperatures of 1329-1706 K with a constant O_2 mole fraction of 0.06. The centerline is defined as the highest intensity location at each downstream distance

Table 2
Combustion study test matrices.

Constant O_2 mole fraction, varying T_{ad}		
φ	T_{ad} [K]	O_2 mole fraction
0.5	1329	0.06
0.52	1430	
0.54	1527	
0.56	1618	
0.57	1645	
0.58	1706	
Constant T_{ad}, varying O_2 mole fraction		
φ	T_{ad} [K]	O_2 mole fraction
0.7	1645	0.04
0.63		0.05
0.57		0.06
0.50		0.09
0.42		0.12
0.35		0.17

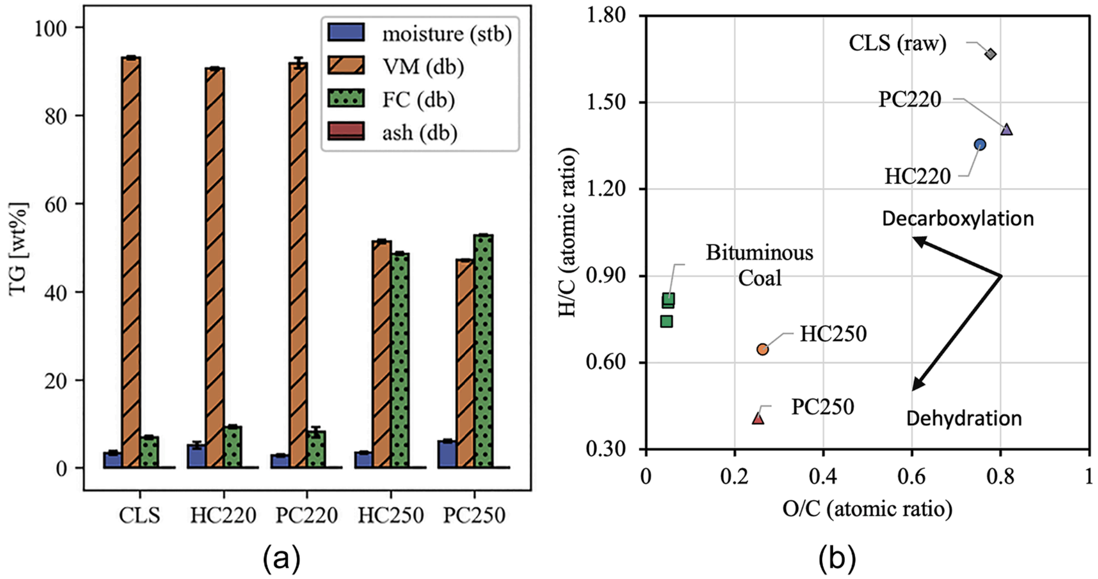

Fig. 3. (a) Proximate analysis and (b) van Krevelen diagram for HCs and PCs. VM is Volatile Matter, FC is Fixed Carbon. In (b), raw cellulose and bituminous coal examples are included for context [73,74].

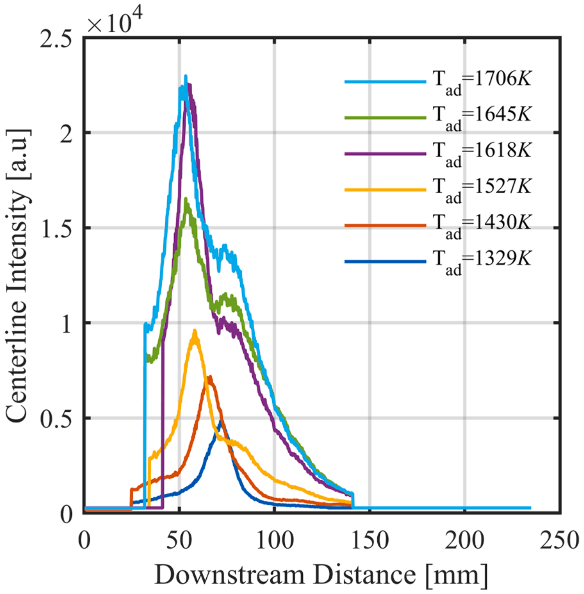

Fig. 4. Time-averaged centerline intensity profiles for HC220 at different T_{ad} under O_2/N_2 environment while O_2 mole fraction is constant.

and the intensity is calculated as the average of that pixel and the one on either side, which avoids issues related to pixel-to-pixel intensity variation. The time-averaged CH* images for all cases are shown in the supplementary material.

Depending on the surrounding gas temperature, CH* profiles exhibit different shapes, which can be linked to the combustion mode. Over this temperature range, CH* intensity profiles display a transition from a unimodal to a bimodal shape. At the lowest temperature, 1329 K, the profile shows a single peak, similar to the cellulose profiles in our previous work [63]. At 1430 K, a subtle shoulder downstream of the peak is discernable, which becomes more pronounced as the temperature increases. Profiles with these two features suggest two different combustion modes; similar intensity profiles were also observed in previous studies of both single particle ignition and streams of particles [28,36]. These previous works showed that the first peak is the result of gas-phase ignition of volatiles and the second peak is the result of heterogeneous combustion of the char residue. To further explain the combustion mode distinction, two-color pyrometry is used. Fig. 5 shows the pyrometric signals superimposed with the CH* intensity profile along the centerline for the 1618 K and 1706 K conditions. At these conditions, the pyrometric signals peak at the region of the second phase of CH* profile, indicating homogeneous ignition.

To better understand the source of the volatiles that drive the initial ignition, we repeat a subset of the combustion experiments with extracted HC, which consists of only the PC and not the SC. Given sample size limitations, two conditions are considered: the baseline, T_{ad}=1645 K, O_2=0.06, and a higher temperature and constant oxygen mole fraction, T_{ad}=1706 K, O_2=0.06. Fig. 6 shows normalized time-averaged CH* profiles for both HC220 and PC220 at (a) baseline and (b) the higher temperature condition. The time-averaged pyrometric profiles in Fig. 6 (c) and (d) are only presented for PC220 for reference.

Fig. 6(a) shows that SC removal delays ignition. At the baseline, the ignition delay times for HC220 and PC220 are 5.69 ms and 18.02 ms, respectively. Additionally, the second peak is less prominent. However, based on Fig. 6(c), the ignition mode is still homogeneous-dominant because the pyrometric signals align with the second CH* peak and not with the initial peak. The higher temperature case also showed a delayed ignition after SC extraction (from 7.30 ms to 22.60 ms), again with a homogeneous-dominant ignition mode based on the pyrometric data shown in Fig. 6(d). Further insight into the impact of the secondary char on ignition comes from DTG profiles for HC220 and PC220 obtained under inert and oxidative atmospheres at a heating rate of 10 K/min, as shown in Fig. 7. DTG curves of oxidation at 50 and 100 K/min heating rates are shown in the supplementary material.

The DTG curves for both as-carbonized (HC220) and primary (PC220) hydrochars suggest two different decomposition modes. The DTG profile of the inert condition for HC220 consists of only one peak related to a significant pyrolysis of HC, which occurs around 600 K. However, under an oxidative atmosphere three peaks can be seen. A very small peak around 500 K is only seen for HC220 under an oxidative atmosphere and is likely the devolatilization and subsequent oxidation of the SC, since the same peak is absent both for the pyrolysis of HC (Fig. 7a) and the pyrolysis and oxidation of PC (Fig. 7b). Elemental analysis shows a more carbonized PC compared to the HC, indicating that SC contains more oxygenated and hydrogenated compounds that volatilize at lower temperatures. This is supported by the analysis of the primary components of the SC from HC220 and HC250 being 5-hydroxymethylfurfural ($C_6H_6O_3$) and levulinic acid ($C_5H_8O_3$), respectively. The DTG peak between 600-650 K (the tallest) is the result of pyrolysis reactions of the volatile matter in the HC. This peak is present in both the pyrolyzing (N_2) and oxidizing (air) atmospheres at essentially the same

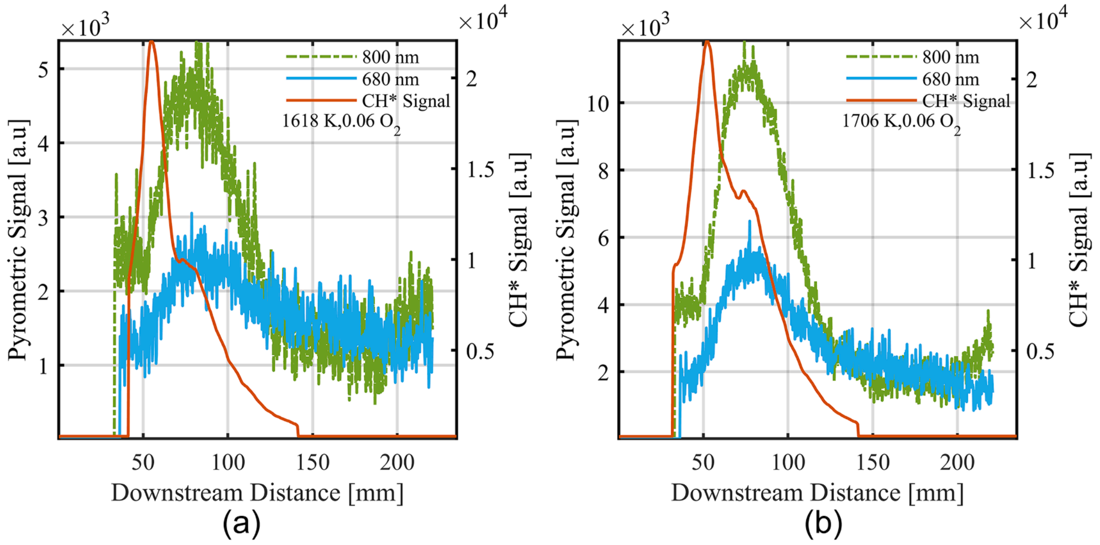

Fig. 5. Time-averaged pyrometric signals superimposed with CH* intensity of HC220 (a) T_{ad} =1618 K and O_2=0.06 (b) T_{ad} =1706 K and O_2=0.06.

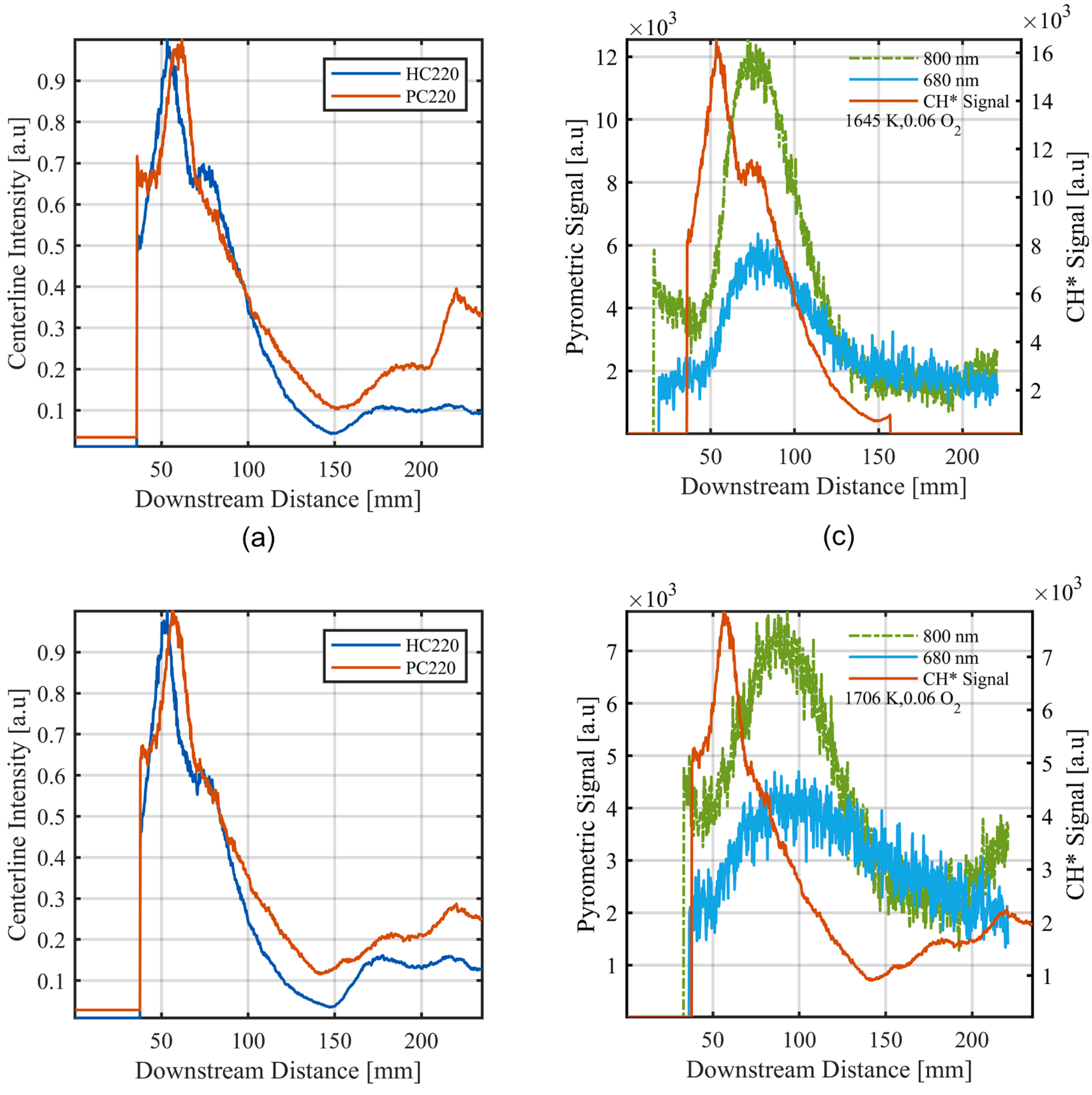

(a)

(c)

(c)

(d)

Fig. 6. Normalized time-averaged CH* intensity profiles for (a) HC220 and PC220 at T_{ad}=1645 K, O_2=0.06, (b) HC220 and PC220 at T_{ad} =1706 K, O_2=0.06. Time-averaged pyrometric signals for PC220 (c) at T_{ad} =1645 K, O_2=0.06, (d) at T_{ad} =1706 K, O_2=0.06.

temperatures, indicating that this peak is due to pyrolysis more so than oxidation. Following the initial devolatilization, the volatiles likely oxidize in air, but that would not be reflected in the TGA signal. The peak between 750-800 K shows the oxidation of the fixed carbon, as it is only present in the oxidative atmosphere for both HC and PC.

CH* and two-color pyrometry results suggest a homogeneous ignition of volatiles followed by a burn-out of the remaining solid phase. Removal of the SC results in delayed ignition, suggesting that the SC devolatilizes more quickly than the PC and provides volatiles for ignition earlier in the process. DTG results show the same role of the SC in devolatilization due to their lower devolatilization temperature. Finally, at low temperatures, a single combustion mode is observed in the CH* data, whereas the solid-phase burning is evident in both the second CH* peak and two-color pyrometry signals at temperatures of 1430 K and above. The low-temperature behavior at 1329 K is very similar to the CH* profiles seen for cellulose in our previous work [63], which suggests that HC220 and raw cellulose behave in a very similar manner. Indeed, HC220 is only slightly more concentrated in elemental carbon than cellulose, as shown in Fig. 3(b), and it shows a very similar DTG profile to cellulose, suggesting a similar devolatilization process. The only difference in the DTG profiles is the presence of a small peak around 800 K that is not present in the inert atmosphere, attributed to the level of carbonization that is present in HC220 and the remaining fixed char.

The same test matrix and analysis is applied to HC250, which is significantly more carbonized. Time-averaged centerline CH* profiles for HC250 at different ambient temperatures are shown in Fig. 8. The full time-averaged CH* images for these cases are provided in the supplementary material.

Over this temperature range, all CH* profiles are clearly bimodal. However, as the temperature increases, the relative amplitude of the first and second CH* signal peaks change. At 1430 K and above, the second peak is higher than the first one. The first peak likely indicates the ignition of volatiles, while the second one is the burning of the condensed phase. To confirm this hypothesis, Fig. 9 shows the time-averaged pyrometric signals with their corresponding CH* profiles for two cases: 1527 K and 1618 K. The remaining cases are similar and presented in the supplementary material. In all cases, the pyrometric signals align with the second peak of the profile, indicating that the initial peak is indicative of volatile ignition and the second peak is indicative of char combustion.

Increasing HTC temperature from 220 to 250°C increased hydrolysis and the condensation of water soluble molecules in the form of SC [17].

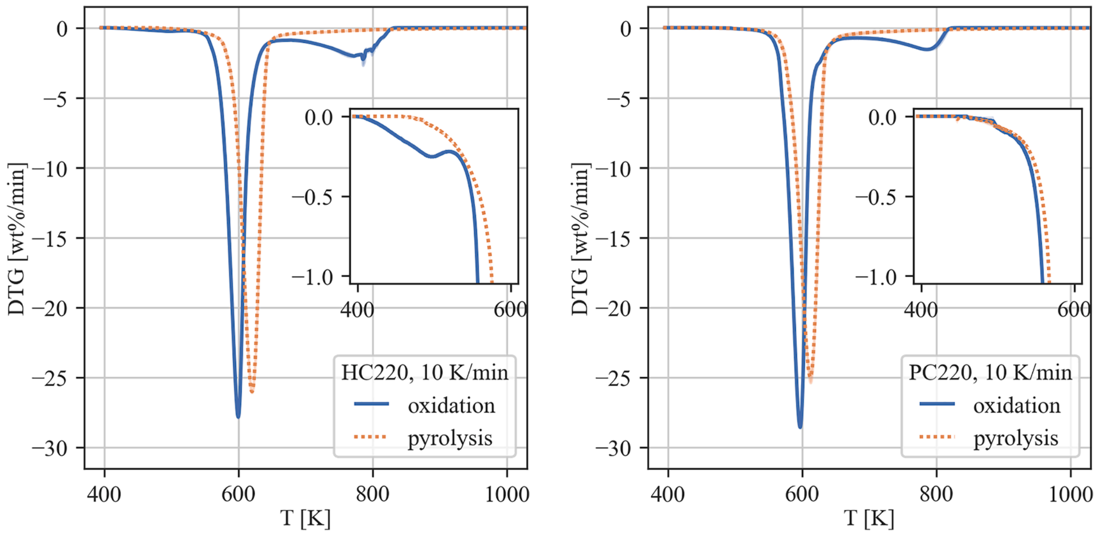

(a)

(b)

Fig. 7. DTG curves for (a) HC220 and (b) PC220 in a pyrolytic and oxidative atmosphere.

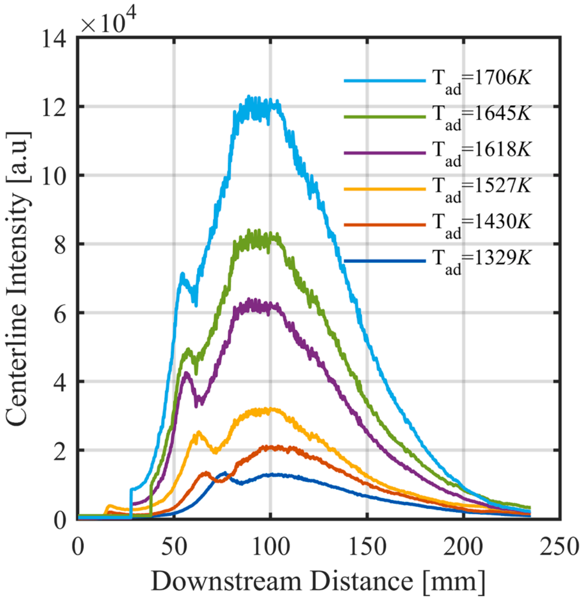

Fig. 8. Time-averaged centerline intensity profiles for HC250 at different T_{ad} under O_2/N_2 environment while O_2 concentration in combustion product is constant.

To understand SC role on volatile ignition for HC250, Fig. 10 compares normalized time-averaged CH* profiles at two conditions: a baseline, T_{ad}=1645 K, O_2=0.06, and higher temperature condition, T_{ad}=1706 K, O_2=0.06. The time-averaged pyrometric profiles in Fig. 10(b) and Fig. 10(d) are presented for PC250.

For the baseline case, in the CH* profile of PC250, the first peak related to the volatile combustion phase disappeared, most likely due to the absence of SC, which would contribute to volatile combustion and result in a bimodal shape. Ignition delay times at the baseline condition for HC250 and PC250 are 9.77 ms and 9.84 ms, respectively. The higher temperature case shows the same trend, except ignition is slightly delayed after SC extraction and is 7.21 ms and 9.45 ms for HC250 and PC250, respectively. It suggests that extraction of SC only has a minor impact on ignition delay time. After SC extraction, the ignition mode remains homogeneous-dominant for both baseline and higher temperature cases. Additional information comes from the DTG curves for HC250 and PC250 under inert and oxidative atmospheres, as presented in Fig. 11. DTG curves of oxidation at higher heating rates of 50 and 100 K/min are shown in the supplementary material.

HC250 and PC250 show similar decomposition behavior in both nitrogen and air atmospheres, with the exception of the presence of a first peak at 450 K of the HC250 case. This peak is attributed to the presence and subsequent devolatilization (and oxidation of volatiles) of SC. The HC and PC decomposition strongly depends on the gas atmosphere. For HC250, the initial peak at 450 K represents SC, whose surface-coating volatiles devolatilize at lower temperatures. This peak is missing in PC250, as the SC was extracted. In the inert atmosphere, both HC250 and PC250 show a peak around 700 K corresponding to pyrolysis of volatile matter. Under an oxidative atmosphere, HC250 and PC250 show two large peaks around 600 and 800 K, roughly attributed to oxidation of volatile matter and fixed carbon, respectively. The difference between inert and oxidative atmospheres indicates that oxidative reactions may enhance VM devolatilization at lower temperatures (potentially through enhanced energy due to oxidation), while PC degradation is mainly oxidation driven. DTG data shown in Fig. 11(b) show that the first peak attributed to the SC in Fig. 11(a) no longer appears, due to SC extraction. In CH* profiles of PC250, the first peaks associated with volatile combustion don't exist, which implies that for HC250, the initial ignition is driven by SC and, based on pyrometric data, the ignition mode remains homogeneous-dominant after SC removal (see Fig. 10(c) and (d)).

The difference in the level of carbonization between HC220 and HC250 has clear effects on the HC behavior in combustion and TGA experiments. The difference can first be seen in the change in the ignition delay time as a function of temperature, which is shown in Fig. 12, where the error bars represent the uncertainty of the measurement explained in detail in the supplementary material. For both materials, the ignition delay time decreases with increasing temperature until temperatures above 1600 K, where the trend plateaus. In the lower temperature ranges, the ignition delay time of the HC220 is less than that of the HC250.

These differences in ignition delay time and combustion behavior between the two materials can be linked to the level of carbonization and the impact that carbonization has on devolatilization and ignition processes. To better understand these differences, comparison between the DTG curves of the two materials, HC220 in Fig. 7 and HC250 in Fig. 11, is instructive. Starting with the DTG curves in the inert

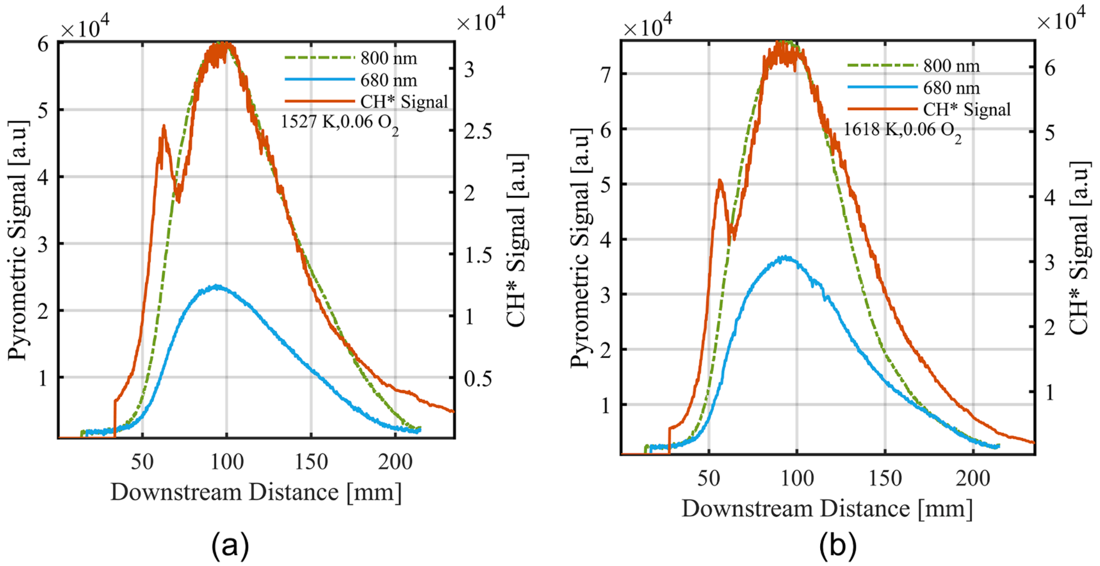

Fig. 9. Time-averaged CH* and pyrometric signals for HC250 for (a) T_{ad}=1527 K, O_2=0.06 and (b) T_{ad}=1618 K, O_2=0.06.

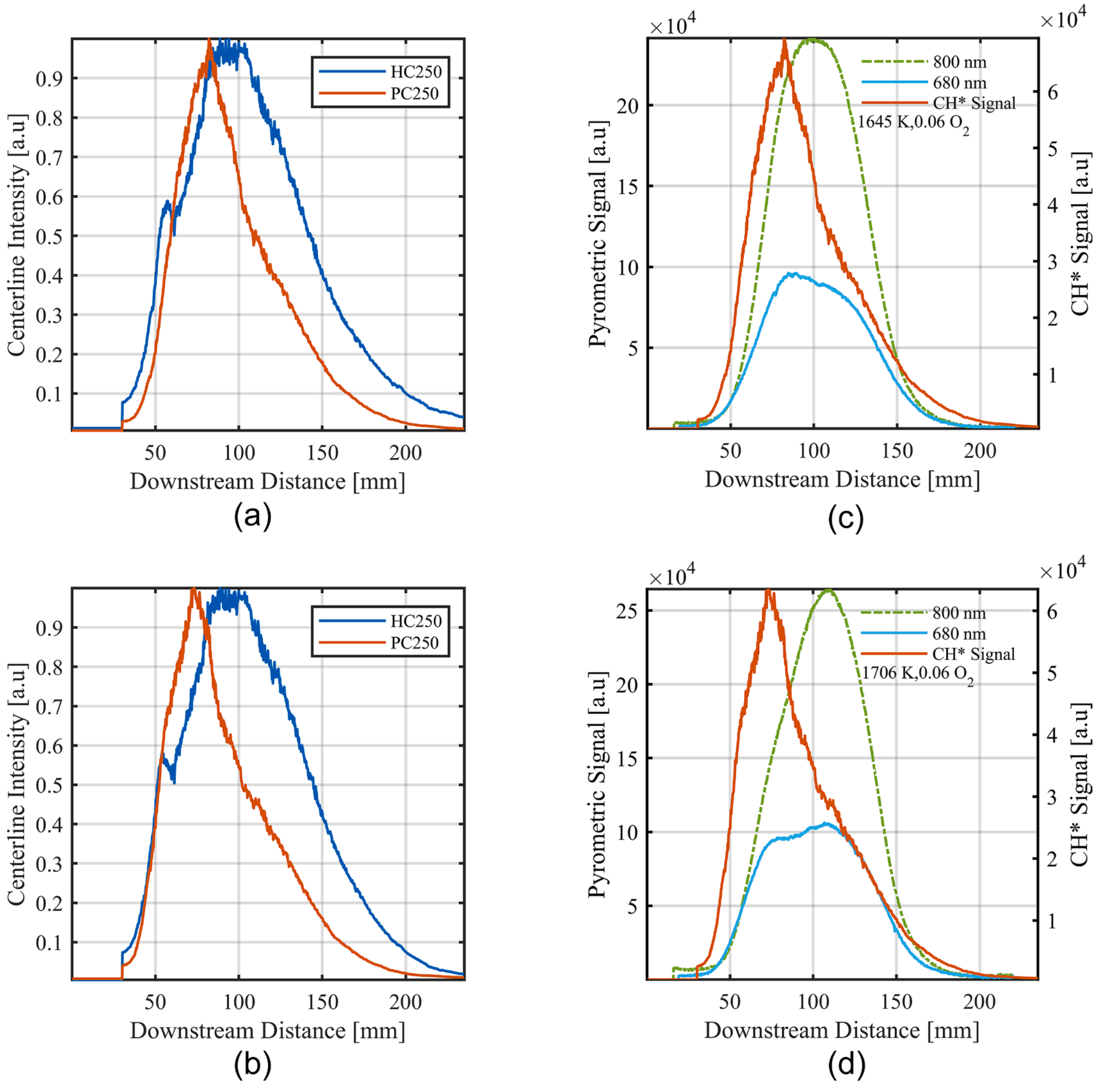

Fig. 10. Normalized time-averaged CH* intensity profiles for (a) HC250 and PC250 at T_{ad}=1645 K, O_2=0.06, (b) HC250 and PC250 at T_{ad}=1706 K, O_2=0.06. Time-averaged pyrometric signals for PC250 (c) at T_{ad}=1645 K, O_2=0.06, (d) at T_{ad}=1706 K, O_2=0.06

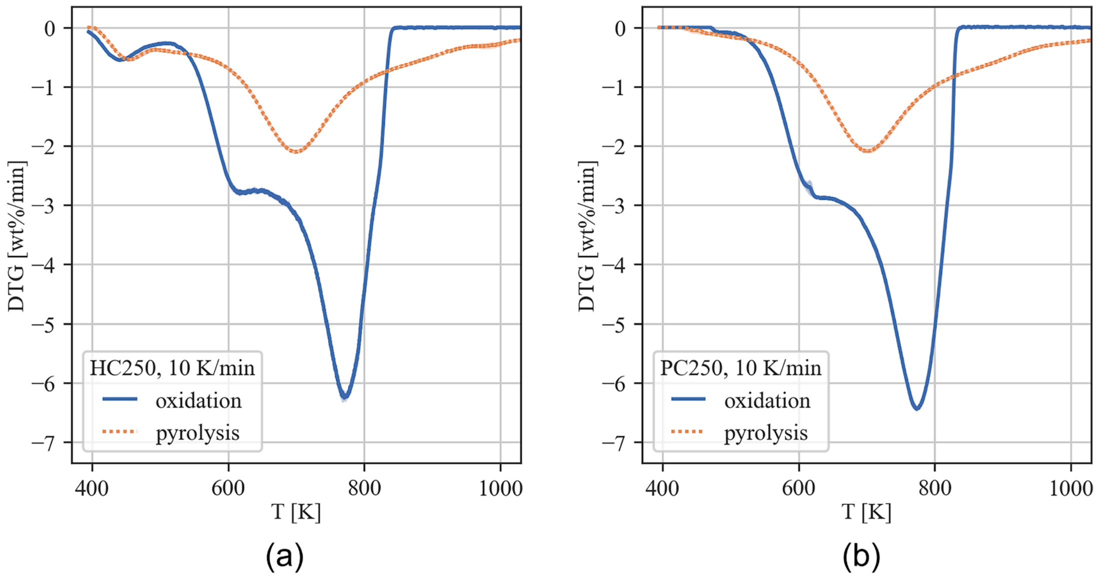

Fig. 11. DTG curves for (a) HC250 and (b) PC250 in an inert and oxidative atmosphere at 10 K/min.

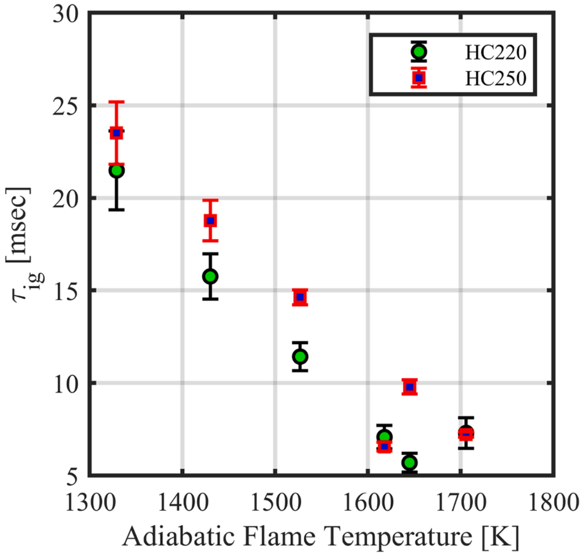

Fig. 12. Ignition delay at different T_{ad} and constant O_2 mole fraction for HC220 and HC250.

atmosphere, the main peak shrinks in height (see y-axis range in plots) and shifts to a higher temperature 700 K for HC250 as compared to HC220. The second peak corresponds to volatile oxidation, seen for both HC220 and HC250, and has a lower intensity for HC250, which is consistent with its lower volatile content. The small peak near 800 K in HC220, indicating char burnout, is the major peak for the oxidative DTG curves of HC250 due to its increased carbonization.

The differences in devolatilization due to the interplay between SC extraction and the level of carbonization are shown in the materials' solid distillation curves in Fig. 13. Temperature profile and DTG curves are shown in Fig. 13(a), while the mass loss at each step (indicated by its maximum temperature) is shown in Fig. 13(b). Six materials are shown: raw cellulose, cellulose put through the same extraction process as the HCs, HC220, PC220, HC250, and PC250. Significant differences between the as-carbonized and extracted HCs, as well as between the two different HCs, are evident in this analysis.

Each temperature step of the distillation process reveals differences between the materials. Only HC220 and HC250 show a mass loss of ~4–5 % at the first temperature of 495 K, due to devolatilization of the SC. The second step (579 K) shows the impact of HTC temperature on the stability of HCs and PCs: HC220 and PC220 show more devolatilization than untreated cellulose, while HC250 and PC250 show considerably less mass loss [17]. This difference suggests that HTC at 220°C can break the cellulose structure, but is not enough for significant repolymerization of aqueous compounds into a more stable, likely aromatic phase, which instead clearly happens at 250°C. The third step (678 K) likely involves breaking glucose chain fragments in the cellulose and is the only step where raw cellulose has greater losses than the other feedstocks [63,73]. Steps at 777 and 876 K show the importance of reaching 250°C during HTC to form a stable carbonaceous core, and peaks are only significantly different for HC250 and PC250. After the last step of distillation, the atmosphere was switched from inert (N_2) to oxidative (air), and the step mass losses agree with our proximate analysis in terms of fixed carbon content remaining in the different samples.

Interestingly, the effect of ethanol extraction is not simply that of removing the most volatile components from the solid surfaces (see the peak at 495 K). For unreacted cellulose and HC220, ethanol extraction decreases the peak at 678 K in favor of the one at 579 K. This result suggests that ethanol can (partially) break the unreacted cellulose structure but cannot do the same for the more carbonaceous core formed through HTC at 250°C.

3.3. *Effects of variations in oxygen mole fraction on ignition mode of HC*

The second test matrix (Table 2) holds the ambient temperature constant while the oxygen mole fraction varies between 4% and 17%. These variations in oxygen mole fraction are expected to have little effect on the devolatilization process but have a significant impact on both the gas- and condensed-phase chemical kinetics. Given the key role that devolatilization plays in the ignition process, as illustrated by the previous test matrix, this test matrix will provide a way to better probe kinetic impacts of HTC severity and extraction. Fig. 14 shows the time-averaged CH* centerline intensity signals of these cases for both as-carbonized HCs. All time-averaged CH* images of both HC220 and HC250 are presented in supplementary material.

The CH* profiles for HC220 and HC250 show a change in shape as O_2 mole fraction increases, implying that ignition process and combustion modes are sensitive to oxygen mole fraction. By elevating the O_2 mole fraction, profiles of CH* shift from a unimodal to a bimodal shape. To provide further clarification on combustion mode transition, the

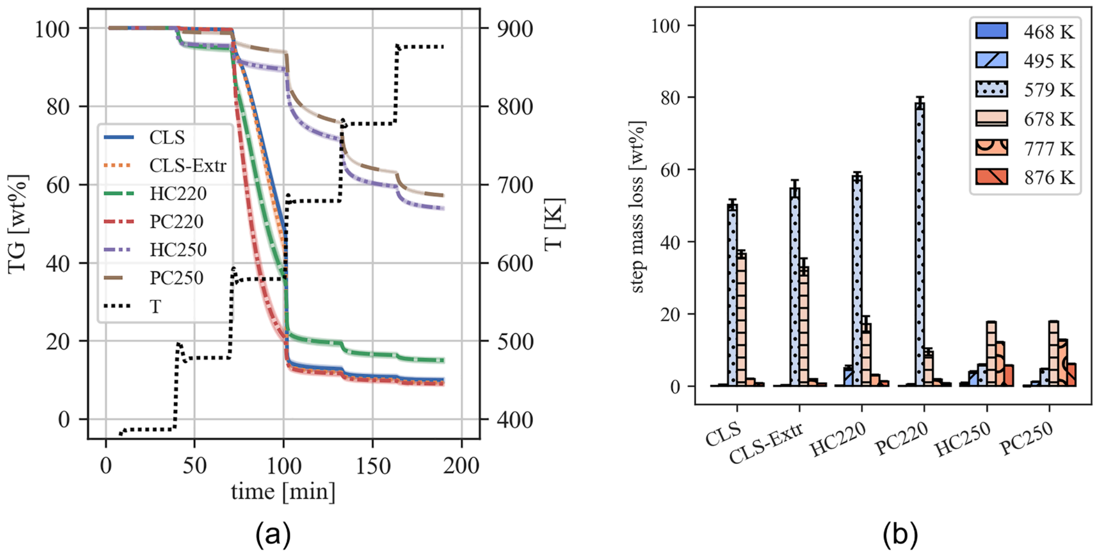

Fig. 13. Solid distillation TG curves (a) and relative mass loss at each temperature step (b) for raw cellulose, ethanol extracted raw cellulose, HCs, and PCs. Curves are on a dry basis. Error represents standard deviation (of triplicates for mass losses, of samples for temperature).

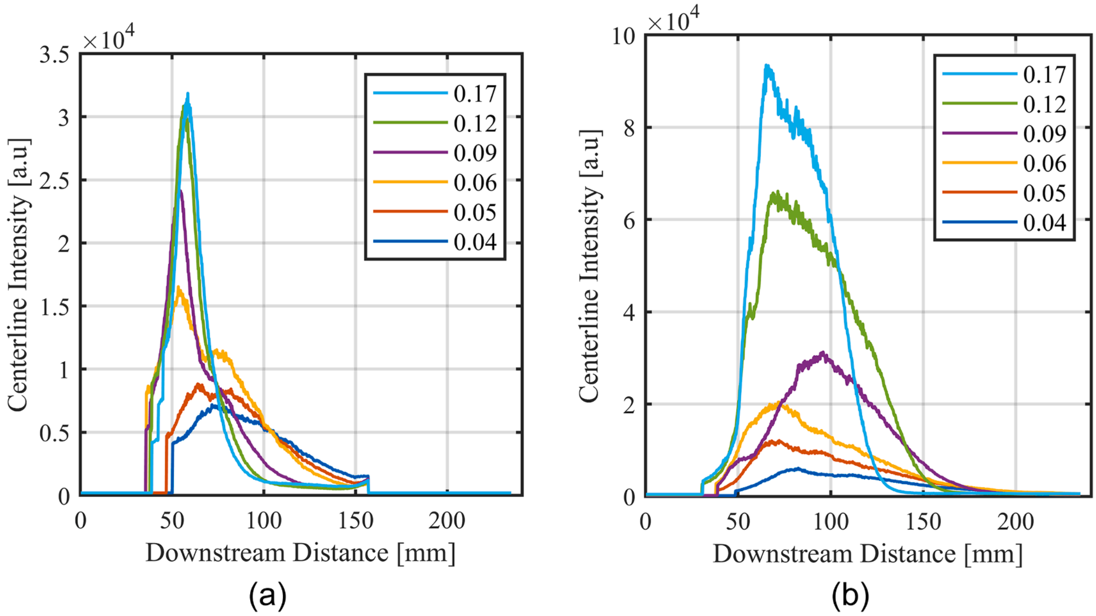

Fig. 14. Time-averaged centerline intensity profiles for (a) HC220 and (b) HC250 with varying O_2 mole fraction at a $T_{ad} = 1645$ K.

pyrometric data is plotted with the CH* intensity profiles for key cases of HC220 and HC250 are depicted in Figs. 15 and 16, respectively. The remaining cases are presented in the supplementary material.

Based on these combined diagnostic results, HC220 experiences a homogeneous-dominant ignition at low O_2 concentration, as evidenced by the delay in the pyrometric signal as compared to the CH* signal. In these cases, sufficient O_2 is not available in the proximity of the particles for significant heterogeneous reactions. This burning mode is similar to the results at the same condition for cellulose discussed in our previous work [63]; companion chemical analysis indicated that ignition of volatile matter at these conditions is very weak due to the very low concentrations of O_2. As O_2 mole fraction increases, kinetic rates for the ignition of volatiles increase, leading to earlier ignition. Further, the combustion of the volatiles heats the particles, leading to more volatile release and faster burning. This behavior is similar to that seen in the DTG results, where the oxidation of HC220 is accelerated by the devolatilization and subsequent oxidation of SC at lower temperatures. At an O_2 mole fraction of 0.05, particles undergo a transition to a bimodal combustion mode and the char phase of combustion is intense enough to be registered in the CH* imaging. The same result is seen for mole fractions of 0.06 and 0.09. The alignment of the pyrometric signal with the second peak of the CH* signal in Fig. 15(b) is further evidence of this combustion mode. At higher levels of oxygen mole fraction (0.12 and 0.17), the CH* profile and the pyrometric signal have a similar shape, where the CH* shows a small shoulder at the beginning of the ignition process and the pyrometric signal is only slightly delayed from the CH* profile. At these conditions, the amount of O_2 in the vicinity of particles is likely sufficient to ignite both the volatiles and the condensed-phase fuel at approximately the same time. The more prominent heterogeneous reaction at higher O_2 levels is evident from a broader coverage between the peak region of the pyrometric signals and CH* profile.

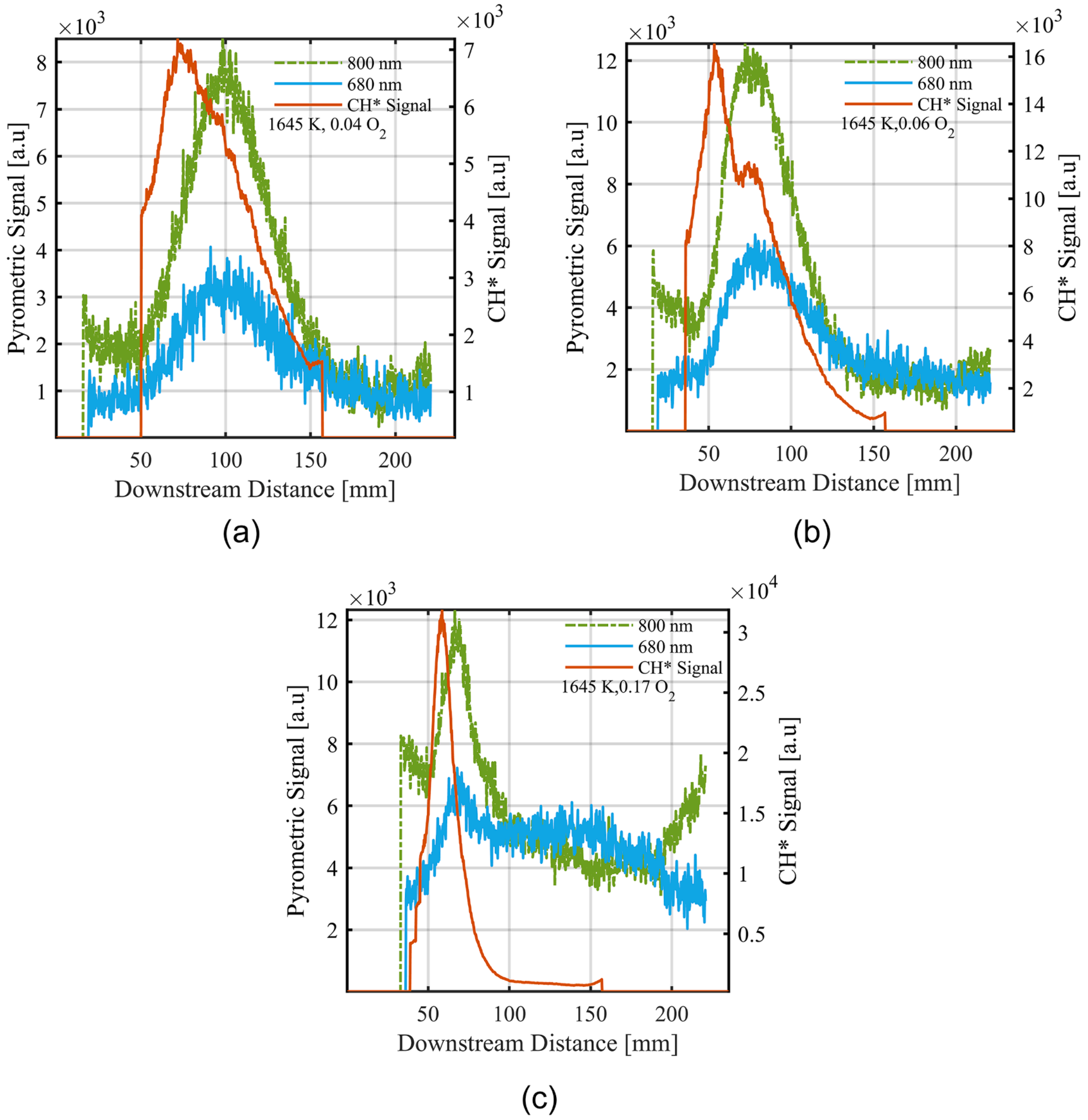

Fig. 15. Time-averaged pyrometric signals superimposed with CH* intensity of HC220 at (a) O_2=0.04 and T_{ad}=1645 K, (b) O_2=0.06 and T_{ad}=1645 K, and (c) O_2=0.17 and T_{ad}=1645 K.

HC250 also displays a transition in behavior with oxygen mole fraction. The CH* profiles at the two lowest O_2 mole fractions (0.04 and 0.05) have a slight shoulder downstream of the first peak. This two-stage combustion behavior is more prominent in the HC250 than in the HC220, likely because of the higher level of carbonization and resulting slower devolatilization. The two-stage combustion is further supported by the significant delay between the CH* and pyrometric signals, as seen in Fig. 16(a) for an oxygen mole fraction of 0.04.

At oxygen mole fractions of 0.09 and above, however, the shape of the CH* profile changes significantly. At these conditions, a very small first peak is followed by a high-amplitude second peak. The pyrometric signals shown in Fig. 16(b) and .(c) essentially overlap with the CH* signals, indicating ignition of the condensed phase; it is not possible to tell if there is also ignition of the volatiles at the same time. These results are similar to those of the transition ignition model first developed by Annamalai et al. [42], which predicted the transition from homogeneous to heterogeneous ignition by increasing the O_2 concentration. In this model, heterogeneous ignition happens when the rate of mass loss due to heterogeneous reactions surpasses the rate of release of volatiles. A critical mass loss rate is defined as the criterion for heterogeneous ignition, which is obtained by applying Semenov's theory of thermal ignition to the energy equation that governs the particle heating rate in a hot oxidizing environment considering heterogeneous heat generation, heat of pyrolysis, conduction, and radiation heat transfer rates. This ignition mode transition from homogeneous to heterogeneous was further evidenced experimentally by previous studies [28].

The effect of SC on combustion behavior of HC220 and HC250 in atmospheres with varying O_2 mole fraction is shown in Fig. 17. Fig. 17 (a) and .(b) show the CH* profiles of HC220, HC250, and their extracted chars at higher O_2 mole fraction as compared to the baseline conditions shown in Figs. 6 and 10, respectively. At higher O_2 mole fractions, HC220 and PC220 have almost identical shapes even though the measured ignition delay times are 7.84 ms to 23.48 ms, respectively. In this case the reason for the delayed ignition is due to the increased residence time of particles as a result of decreased particle fluidization, not because of any alteration in the ignition location or profile shape. CH* profiles suggest that the secondary char does not play as important a role in ignition at high-oxygen conditions as it does with variations in temperature, likely because changing the mole fraction of O_2 does not significantly impact the devolatilization process of SC or PC. Comparing the shapes of HC250 and PC250 indicates that the SC does drive the initial ignition. At higher O_2 concentrations, the ignition mode of PC250

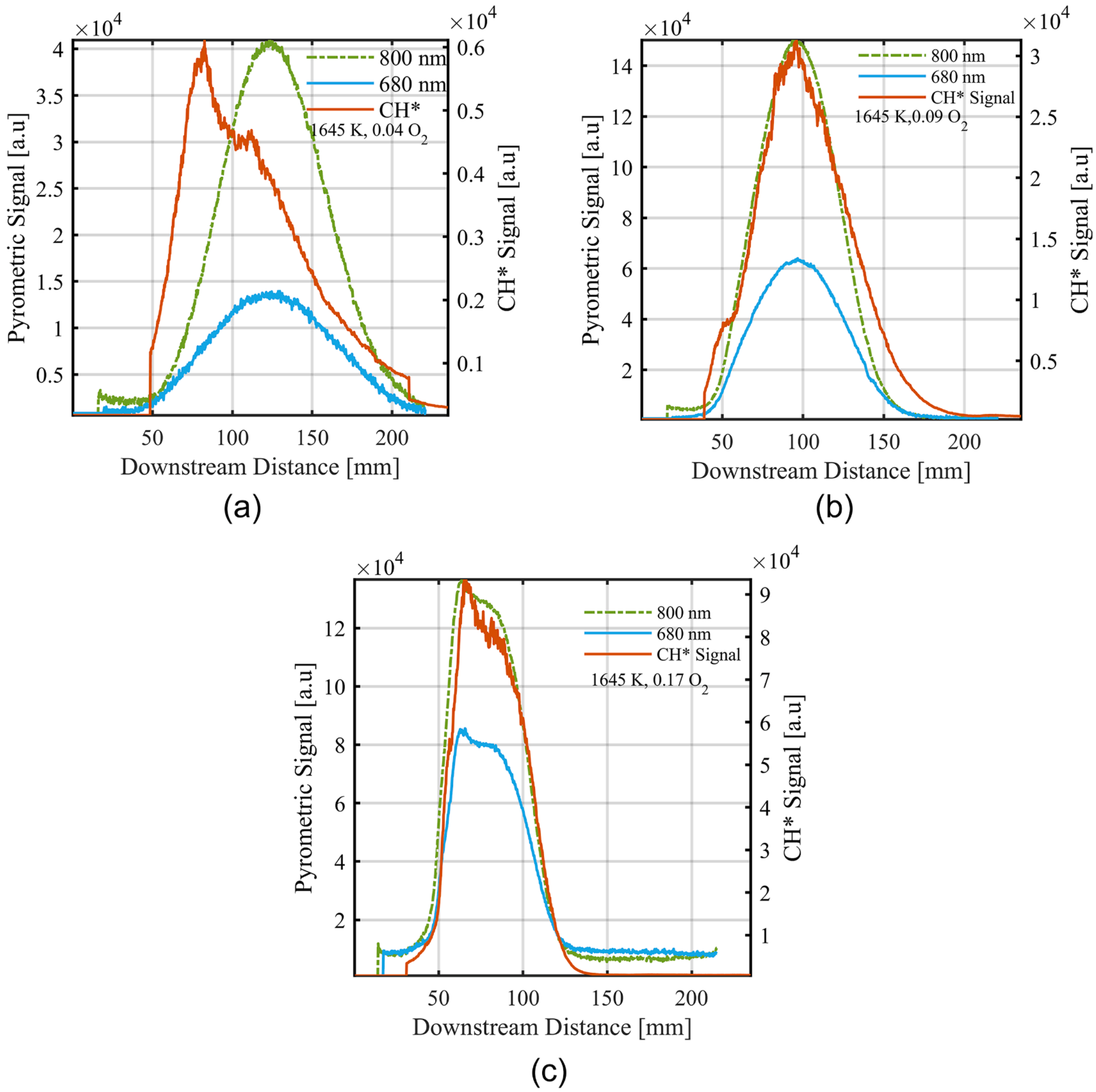

Fig. 16. Time-averaged pyrometric signals superimposed with CH* intensity of HC250 at (a) O_2=0.04 and T_{ad}=1645 K, (b) O_2=0.06 and T_{ad}=1645 K, and (c) O_2=0.17 and T_{ad}=1645 K.

is heterogeneous-dominant, as indicated by the disappearance of the first small peak, likely because SC was removed, and the ignition was delayed from 10.52 ms to 15.54 ms.

Ignition delay times for both as-carbonized HCs as a function of oxygen mole fraction are presented in Fig. 18. In all cases, HC220 has a significantly shorter ignition delay time than HC250. However, the ignition delay times for both materials show an interesting trend with oxygen mole fraction. The ignition delay time first decreases then increases with oxygen mole fraction, where the minimum ignition delay time for HC220 is at an O_2 mole fraction of 0.06 and the minimum ignition delay time for HC250 is at an O_2 mole fraction of 0.12. This change in the ignition delay time dependence on O_2 mole fraction is likely a result of the change in burning mode, as these trends align with the shape transitions of the CH* profiles in Fig. 15 and 16. In the first regime where ignition delay time decreases with increasing O_2 mole fraction, the ignition process is homogeneous; in these cases, the homogeneous ignition of hydrocarbon volatiles is promoted by higher O_2 concentrations. However, when the ignition mode starts to include significant contributions from heterogeneous ignition, the trend changes such that ignition delay time increases with increasing O_2 mole fraction. A similar result was observed in previous works [28,42,74], which indicated that a sufficiently high O_2 concentration can move the reaction zone of gaseous volatiles closer to the particle surface, which increases the heat loss from the reaction surface to the particle surface. This heat loss increases the ignition delay time. Further, the oxygen can reach the particle surface, where the homogeneous volatile flame is weak and heterogeneous reactions start to occur. Therefore, the ignition time may increase in high O_2 conditions. These effects are exaggerated as the level of carbonization increases, where the increasing trend of ignition delay time with O_2 mole fraction begins at higher level of oxygen concentration probably due to lower reactivity of the condensed-phase in HC250. The lower reactivity of HC250 compared to HC220 is explained by the lower O/C atomic ratio of HC250, which is almost three times smaller than HC220 based on Fig. 3.

TGA-calculated ignition temperatures $T_{i\text{-}TGA}$ (using oxidation curves obtained at 10 K/min with a threshold of 10 % of the maximum peak to identify $T_{i\text{-}TGA}$) showed similar values for HCs and PCs obtained at the same temperatures (~640 K for HC220 and PC220; ~570 K for HC250 and PC250). The inverse trend of $T_{i\text{-}TGA}$ (HC220 > HC250) with respect to ignition delay obtained in the Hencken burner (HC220 < HC250) suggests $T_{i\text{-}TGA}$ might not be a good proxy for its combustion counterpart. However, we highlight the necessity of expanding this analysis to a larger sample set to draw definitive conclusions.

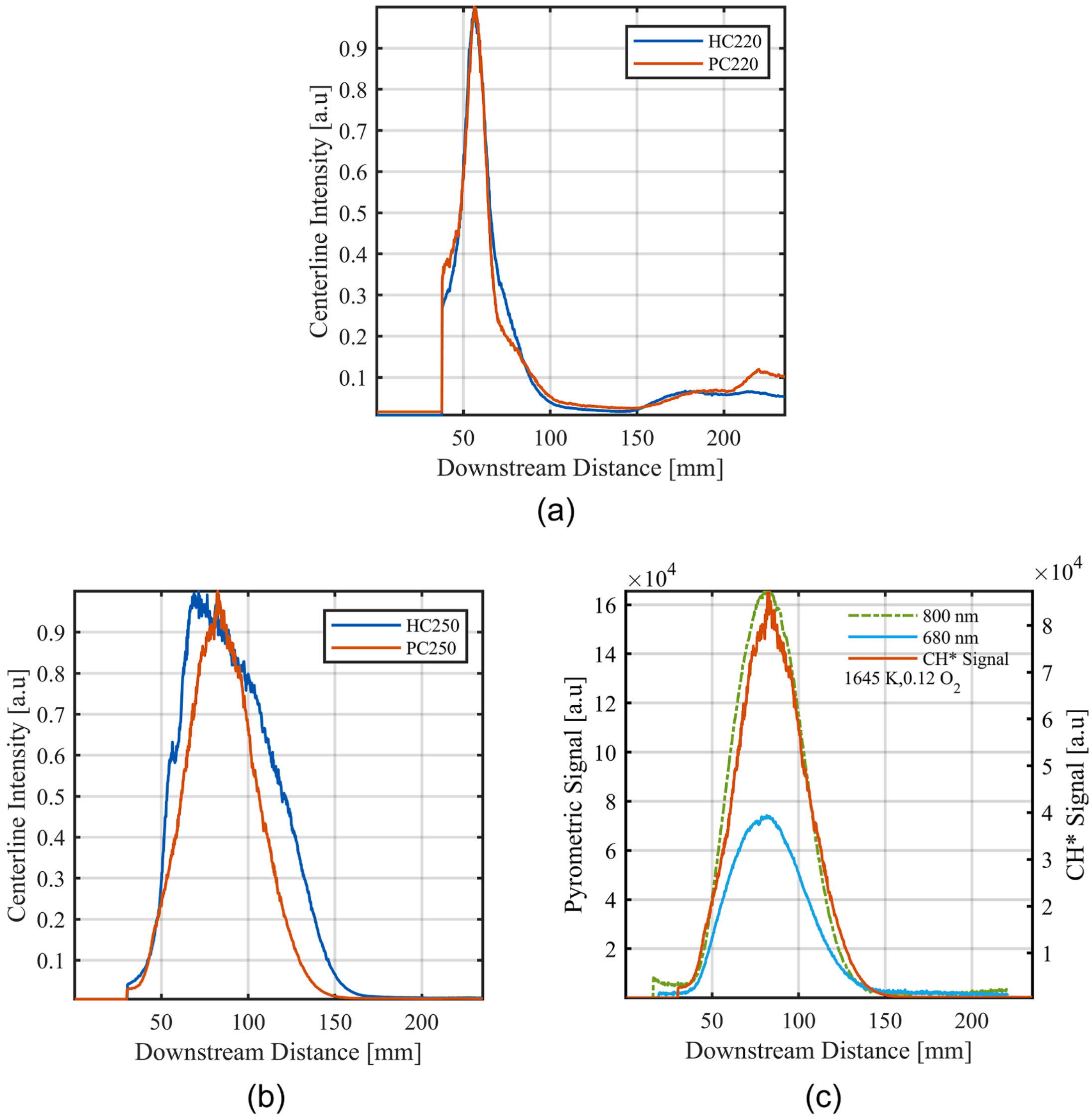

Fig. 17. Normalized time-averaged CH* intensity profiles for (a) HC220 and PC220 at T_{ad}=1645 K, O_2=0.12, (b) HC250 and PC250 at T_{ad}=1645 K, O_2=0.12. Time-averaged CH* and pyrometric signals for PC250 (c) at T_{ad}=1645 K, O_2=0.12.

4. Conclusions

The combustion behavior of cellulose HC (produced at two temperatures) and PC (extracted using ethanol) were investigated using a Hencken burner and coupled with thermogravimetric analysis. Combustion experiments used a unique combination of diagnostics to quantify ignition delay time and identify combustion modes. HC combustion processes depend on the volatile matter, ambient temperature, and oxygen concentration in the surrounding atmosphere. Less carbonized HC220, which contains more than 80 % volatile matter, ignites homogeneously even under low temperature regimes, exhibiting a transition from single-mode combustion to a double-mode combustion as temperature increases. The more carbonized HC250 and PC250, with around 50% volatile matter, showed a greater tendency towards heterogeneous combustion. Oxygen has a more complicated effect on ignition and combustion modes, as HCs revealed combustion and ignition mode transition attributed to an increase in oxygen mole fraction. Despite it comprising a relatively small mass percentage of HC, (below 30%) secondary char contributes significantly to the initial gas-phase ignition, leading to a faster ignition due to its low devolatilization temperature (under 495 K). These findings provide a fundamental foundation on which further studies of this promising biofuel can be built.

This study marks one of the first attempts to harmoniously characterize the ignition and combustion behavior of biomass-based hydrochars from both fuel science and combustion science perspectives. The highly volatile secondary char has a significant impact on ignition delay times, which is mirrored in thermogravimetric observations. The combined use of combustion experiments and TGA provided critical information about the devolatilization processes, which are shown to be a rate-limiting step for the ignition of these fuels. Further, the level of carbonization, a result of the HTC process temperature, had a significant impact on the combustion mode, particularly the prevalence of heterogeneous reactions. Lower HTC temperatures result in higher yields and lower levels of carbonization, resulting in somewhat similar combustion properties between the feedstock material and the hydrochar. Higher HTC temperatures result in lower yields but higher levels of carbonization. More testing of these fuels in realistic burner geometries and in comparison to a variety of solid fuels will provide better information about the suitability of these fuels for different solid-fuel combustion applications.

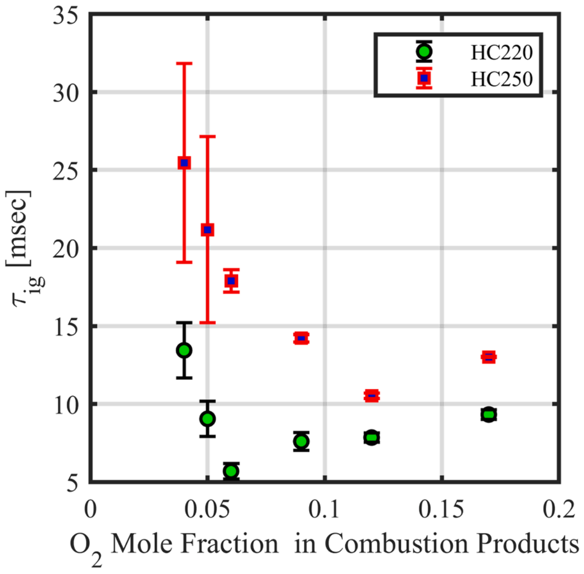

Fig. 18. Ignition delay at different O_2 levels and constant T_{ad}=1645 K for HC220 and HC250.

Novelty and significance statement

This is one of the first characterizations of the combustion behavior of hydrochar, a promising biofuel. The combustion experiments are designed to understand the relative importance of different rate-limiting processes, including solid fuel devolatilization and ignition. Further, highly coupled combustion experiments and thermogravimetric analysis are used to better understand the combustion behaviors of this fuel and the role of secondary char. This combined methodology provides a pathway for more thorough analysis of combustion behaviors of a wide range of renewable solid fuels.

CRediT authorship contribution statement

Parvaneh Motiei: Writing – original draft, Methodology, Investigation, Formal analysis, Data curation, Conceptualization. **Matteo Pecchi:** Writing – original draft, Methodology, Investigation, Formal analysis, Data curation, Conceptualization. **James L. Adair:** Writing – original draft, Methodology, Formal analysis, Data curation, Conceptualization. **Jillian L. Goldfarb:** Writing – review & editing, Supervision, Project administration, Methodology, Investigation, Funding acquisition, Conceptualization. **Jacqueline O'Connor:** Writing – review & editing, Project administration, Investigation, Funding acquisition, Conceptualization.

Declaration of competing interest

The authors declare that they have no known competing financial interests or personal relationships that could have appeared to influence the work reported in this paper.

Acknowledgements

The authors gratefully acknowledge financial support from National Science Foundation (NSF), grant numbers CBET-2031710 and CBET-2031916.

Supplementary materials

Supplementary material associated with this article can be found, in the online version, at 10.1016/j.combustflame.2024.113703.

References

[1] R.S. Dhillon, G. von Wuehlisch, Mitigation of global warming through renewable biomass, BioMass BioEnergy 48 (2013) 75–89, https://doi.org/10.1016/j.biombioe.2012.11.005.

[2] Z. Yao, X. Ma, Y. Lin, Effects of hydrothermal treatment temperature and residence time on characteristics and combustion behaviors of green waste, Appl. Therm. Eng. 104 (2016) 678–686, https://doi.org/10.1016/j.applthermaleng.2016.05.111.

[3] L. Gao, M. Volpe, M. Lucian, L. Fiori, J.L. Goldfarb, Does hydrothermal carbonization as a biomass pretreatment reduce fuel segregation of coal-biomass blends during oxidation? Energy Convers. Manage 181 (2019) 93–104, https://doi.org/10.1016/j.enconman.2018.12.009.

[4] E. Monedero, M. Lapuerta, A. Pazo, L.A. Díaz-Robles, E. Pino-Cortés, V. Campos, F. Vallejo, F. Cubillos, J. Gómez, Effect of hydrothermal carbonization on the properties, devolatilization, and combustion kinetics of Chilean biomass residues, BioMass BioEnergy 130 (2019) 105387, https://doi.org/10.1016/j.biombioe.2019.105387.

[5] T. Liu, Q. Lang, Y. Xia, Z. Chen, D. Li, J. Ma, C. Gai, Z. Liu, Combination of hydrothermal carbonization and oxy-fuel combustion process for sewage sludge treatment: Combustion characteristics and kinetics analysis, Fuel 242 (2019) 265–276, https://doi.org/10.1016/j.fuel.2019.01.035.

[6] M. Mäkelä, V. Benavente, A. Fullana, Hydrothermal carbonization of lignocellulosic biomass: Effect of process conditions on hydrochar properties, Appl. Energy 155 (2015) 576–584, https://doi.org/10.1016/j.apenergy.2015.06.022.

[7] A. Kruse, F. Koch, K. Stelzl, D. Wüst, M. Zeller, Fate of nitrogen during hydrothermal carbonization, Energy Fuels 30 (2016) 8037–8042, https://doi.org/10.1021/acs.energyfuels.6b01312.

[8] A. Kruse, A. Funke, M.-M. Titirici, Hydrothermal conversion of biomass to fuels and energetic materials, Curr. Opin. Chem. Biol. 17 (2013) 515–521, https://doi.org/10.1016/j.cbpa.2013.05.004.

[9] M. Lucian, M. Volpe, L. Gao, G. Piro, J.L. Goldfarb, L. Fiori, Impact of hydrothermal carbonization conditions on the formation of hydrochars and secondary chars from the organic fraction of municipal solid waste, Fuel 233 (2018) 257–268, https://doi.org/10.1016/j.fuel.2018.06.060.

[10] B. Zhao, H. Wang, S. Xu, L. Qian, H. Li, J. Gao, G. Zhao, M.B. Ray, C.C. Xu, Influence of extraction solvents on the recovery yields and properties of bio-oils from woody biomass liquefaction in sub-critical water, ethanol or water–ethanol mixed solvent, Fuel 307 (2022) 121930, https://doi.org/10.1016/j.fuel.2021.121930.

[11] T. Wang, Y. Zhai, Y. Zhu, C. Li, G. Zeng, A review of the hydrothermal carbonization of biomass waste for hydrochar formation: Process conditions, fundamentals, and physicochemical properties, Renew. Sustain. Energy Rev. 90 (2018) 223–247, https://doi.org/10.1016/j.rser.2018.03.071.

[12] Y. Lin, X. Ma, X. Peng, Z. Yu, S. Fang, Y. Lin, Y. Fan, Combustion, pyrolysis and char CO2-gasification characteristics of hydrothermal carbonization solid fuel from municipal solid wastes, Fuel 181 (2016) 905–915, https://doi.org/10.1016/j.fuel.2016.05.031.

[13] Y. Gao, X. Wang, J. Wang, X. Li, J. Cheng, H. Yang, H. Chen, Effect of residence time on chemical and structural properties of hydrochar obtained by hydrothermal carbonization of water hyacinth, Energy 58 (2013) 376–383, https://doi.org/10.1016/j.energy.2013.06.023.

[14] B.M. Ghanim, D.S. Pandey, W. Kwapinski, J.J. Leahy, Hydrothermal carbonisation of poultry litter: Effects of treatment temperature and residence time on yields and chemical properties of hydrochars, Bioresour. Technol. 216 (2016) 373–380, https://doi.org/10.1016/j.biortech.2016.05.087.

[15] D. Kalderis, M.S. Kotti, A. Méndez, G. Gascó, Characterization of hydrochars produced by hydrothermal carbonization of rice husk, Solid Earth 5 (2014) 477–483, https://doi.org/10.5194/se-5-477-2014.

[16] L. Zhang, S. Liu, B. Wang, Q. Wang, G. Yang, J. Chen, Effect of residence time on hydrothermal carbonization of corn cob residual, Bioresources 10 (2015) 3979–3986.

[17] M. Pecchi, A. Cascioli, A.R. Maag, J.L. Goldfarb, M. Baratieri, Uncovering the transition between hydrothermal carbonization and liquefaction using differential scanning calorimetry, Fuel Process. Technol. 235 (2022) 107349, https://doi.org/10.1016/j.fuproc.2022.107349.

[18] M. Pecchi, M. Baratieri, A.R. Maag, J.L. Goldfarb, Uncovering the transition between hydrothermal carbonization and liquefaction via secondary char extraction: A case study using food waste, Waste Manage 168 (2023) 281–289, https://doi.org/10.1016/j.wasman.2023.06.009.

[19] M. Pecchi, M. Baratieri, J.L. Goldfarb, A.R. Maag, Effect of solvent and feedstock selection on primary and secondary chars produced via hydrothermal carbonization of food wastes, Bioresour. Technol. 348 (2022) 126799, https://doi.org/10.1016/j.biortech.2022.126799.

[20] C. Zhang, G. Wang, X. Ning, J. Zhang, C. Wang, Numerical simulation of combustion behaviors of hydrochar derived from low-rank coal in the raceway of blast furnace, Fuel 278 (2020) 118267, https://doi.org/10.1016/j.fuel.2020.118267.

[21] T. Eckhard, C. Pflieger, S. Schmidt, J. Böttger, O. Senneca, M. Schiemann, V. Scherer, M. Muhler, F. Cerciello, Catalytic effects for cellulose-based model fuels under low and high heating rate in air and oxy-fuel atmosphere, Fuel 324 (2022) 124437, https://doi.org/10.1016/j.fuel.2022.124437.

[22] H. Düdder, A. Wütscher, N. Vorobiev, V. Scherer, M. Muhler, Oxidation characteristics of a cellulose-derived hydrochar in thermogravimetric and laminar flow burner experiments, Fuel Process. Technol. 148 (2016) 85–90.

[23] Z. Lu, X. Li, J. Jian, S. Yao, Flame combustion of single wet-torrefied wood particle: Effects of pretreatment temperature and residence time, Fuel 250 (2019) 160–167, https://doi.org/10.1016/j.fuel.2019.03.102.

[24] D. Nguyen, W. Zhao, M. Mäkelä, Z.T. Alwahabi, C.W. Kwong, Effect of hydrothermal carbonisation temperature on the ignition properties of grape marc hydrochar fuels, Fuel 313 (2022) 122668, https://doi.org/10.1016/j.fuel.2021.122668.

[25] A. Molina, C.R. Shaddix, Ignition and devolatilization of pulverized bituminous coal particles during oxygen/carbon dioxide coal combustion, Proc. Combust. Inst. 31 (2007) 1905–1912, https://doi.org/10.1016/j.proci.2006.08.102.

[26] L. Zhang, E. Binner, Y. Qiao, C.-Z. Li, In situ diagnostics of Victorian brown coal combustion in O2/N2 and O2/CO2 mixtures in drop-tube furnace, Fuel 89 (2010) 2703–2712, https://doi.org/10.1016/j.fuel.2010.04.020.

[27] R. Khatami, Y.A. Levendis, On the deduction of single coal particle combustion temperature from three-color optical pyrometry, Combust. Flame 158 (2011) 1822–1836, https://doi.org/10.1016/j.combustflame.2011.01.007.

[28] Y. Yuan, S. Li, G. Li, N. Wu, Q. Yao, The transition of heterogeneous–homogeneous ignitions of dispersed coal particle streams, Combust. Flame 161 (2014) 2458–2468, https://doi.org/10.1016/j.combustflame.2014.03.008.

[29] Y.A. Levendis, K. Joshi, R. Khatami, A.F. Sarofim, Combustion behavior in air of single particles from three different coal ranks and from sugarcane bagasse, Combust. Flame 158 (2011) 452–465.

[30] P.E. Mason, L.I. Darvell, J.M. Jones, M. Pourkashanian, A. Williams, Single particle flame-combustion studies on solid biomass fuels, Fuel 151 (2020) 21–30, https://doi.org/10.1016/j.fuel.2014.11.088.

[31] G. Simões, D. Magalhães, M. Rabaçal, M. Costa, Effect of gas temperature and oxygen concentration on single particle ignition behavior of biomass fuels, Proc. Combust. Inst. 36 (2017) 2235–2242, https://doi.org/10.1016/j.proci.2016.06.102.

[32] H. Lee, S. Choi, Volatile flame visualization of single pulverized fuel particles, Powder. Technol. 333 (2018) 353–363.

[33] G.-M. Kim, J.H. Choi, C.-H. Jeon, D.-H. Lim, Effects of Cofiring Coal and Biomass Fuel on the Pulverized Coal Injection Combustion Zone in Blast Furnaces, Energies. (Basel) 15 (2022) 655.

[34] H. Lee, S. Choi, An observation of combustion behavior of a single coal particle entrained into hot gas flow, Combust. Flame 162 (2015) 2610–2620, https://doi.org/10.1016/j.combustflame.2015.03.010.

[35] Y. Yuan, S. Li, F. Zhao, Q. Yao, M.B. Long, Characterization on hetero-homogeneous ignition of pulverized coal particle streams using CH* chemiluminescence and 3 color pyrometry, Fuel 184 (2016) 1000–1006, https://doi.org/10.1016/j.fuel.2015.11.032.

[36] A. Adeosun, Z. Xiao, Z. Yang, Q. Yao, R.L. Axelbaum, The effects of particle size and reducing-to-oxidizing environment on coal stream ignition, Combust. Flame 195 (2018) 282–291, https://doi.org/10.1016/j.combustflame.2018.05.003.

[37] R. Khatami, C. Stivers, K. Joshi, Y.A. Levendis, A.F. Sarofim, Combustion behavior of single particles from three different coal ranks and from sugar cane bagasse in O2/N2 and O2/CO2 atmospheres, Combust. Flame 159 (2012) 1253–1271.

[38] W. Weng, M. Costa, M. Aldén, Z. Li, Single particle ignition and combustion of pulverized pine wood, wheat straw, rice husk and grape pomace, Proc. Combust. Inst. 37 (2019) 2663–2671.

[39] S. Wang, C. Zou, H. Yang, C. Lou, S. Cheng, C. Peng, C. Wang, H. Zou, Bioresource Technology Effects of cellulose, hemicellulose, and lignin on the combustion behaviours of biomass under various oxygen concentrations, Bioresour. Technol. 320 (2021) 124375, https://doi.org/10.1016/j.biortech.2020.124375.

[40] Y. Jia, Z. Li, Y. Wang, X. Wang, C. Lou, B. Xiao, M. Lim, Visualization of Combustion Phases of Biomass Particles: Effects of Fuel Properties, ACS. Omega 6 (2021) 27702–27710.

[41] J. Köser, T. Li, N. Vorobiev, A. Dreizler, M. Schiemann, B. Böhm, Multi-parameter diagnostics for high-resolution in-situ measurements of single coal particle combustion, Proc. Combust. Inst. 37 (2019) 2893–2900, https://doi.org/10.1016/j.proci.2018.05.116.

[42] X. Du, K. Annamalai, The transient ignition of isolated coal particle, Combust. Flame 97 (1994) 339–354, https://doi.org/10.1016/0010-2180(94)90025-6.

[43] S. Kang, X. Li, J. Fan, J. Chang, Characterization of hydrochars produced by hydrothermal carbonization of lignin, cellulose, D-xylose, and wood meal, Ind. Eng. Chem. Res. 51 (2012) 9023–9031, https://doi.org/10.1021/ie300565d.

[44] L. Chen, C. Wen, W. Wang, T. Liu, E. Liu, H. Liu, Z. Li, Combustion behaviour of biochars thermally pretreated via torrefaction, slow pyrolysis, or hydrothermal carbonisation and co-fired with pulverised coal, Renew. Energy 161 (2020) 867–877, https://doi.org/10.1016/j.renene.2020.06.148.

[45] M. Liu, X. Zhu, R. Chen, Q. Liao, A. Xia, Y. Huang, Influence of torrefaction, hydrothermal carbonization and degradative solvent extraction pretreatments on moisture absorption and self-ignition characteristics of biomass, Fuel 282 (2020) 118843, https://doi.org/10.1016/j.fuel.2020.118843.

[46] A. Magdziarz, M. Wilk, M. Wądrzyk, Pyrolysis of hydrochar derived from biomass–Experimental investigation, Fuel 267 (2020) 117246, https://doi.org/10.1016/j.fuel.2020.117246.

[47] M. Volpe, A. Messineo, M. Mäkelä, M.R. Barr, R. Volpe, C. Corrado, L. Fiori, Reactivity of cellulose during hydrothermal carbonization of lignocellulosic biomass, Fuel Process. Technol. 206 (2020) 106456, https://doi.org/10.1016/j.fuproc.2020.106456.

[48] C. Chen, W. Liang, F. Fan, C. Wang, The effect of temperature on the properties of hydrochars obtained by hydrothermal carbonization of waste camellia oleifera shells, ACS. Omega 6 (2021) 16546–16552, https://doi.org/10.1021/acsomega.1c01787.

[49] R. Ma, S. Fakudze, Q. Shang, Y. Wei, J. Chen, C. Liu, J. Han, Q. Chu, Catalytic hydrothermal carbonization of pomelo peel for enhanced combustibility of coal/hydrochar blends and reduced CO2 emission, Fuel 304 (2021) 121422, https://doi.org/10.1016/j.fuel.2021.121422.

[50] S. Poomsawat, W. Poomsawat, Analysis of hydrochar fuel characterization and combustion behavior derived from aquatic biomass via hydrothermal carbonization process, Case Studies in Thermal Engineering 27 (2021) 101255. https://doi.org/10.1016/j.csite.2021.101255.

[51] Y. Zhang, I. Zahid, A. Danial, J. Minaret, Y. Cao, A. Dutta, Hydrothermal carbonization of miscanthus: Processing, properties, and synergistic co-combustion with lignite, Energy 225 (2021) 120200, https://doi.org/10.1016/j.energy.2021.120200.

[52] Y. Ding, D. Li, X. Zhang, M. Lv, S. Qin, P. Zhao, C. Guo, Research on the co-combustion characteristics and kinetics of rice husk hydrochar with anthracite, Energy 299 (2024) 131339, https://doi.org/10.1016/j.energy.2024.131339.

[53] R. Wang, X. Zheng, Z. Feng, Y. Feng, Z. Ying, B. Wang, B. Dou, Hydrothermal carbonization of Chinese medicine residues: Formation of humic acids and combustion performance of extracted hydrochar, Sci. Total. Environ. 925 (2024) 171792, https://doi.org/10.1016/j.scitotenv.2024.171792.

[54] R.Y. Spitzer, Y.Z. Belete, R. Sharon-Gojman, R. Posmanik, A. Gross, Biocrude extraction from human-excreta-derived hydrochar for sustainable energy and agricultural applications, Environ. Res. 247 (2024) 118287, https://doi.org/10.1016/j.envres.2024.118287.

[55] K.Le Manquais, C. Snape, I. McRobbie, J. Barker, V. Pellegrini, Comparison of the combustion reactivity of TGA and drop tube furnace chars from a bituminous coal, Energy Fuels 23 (2009) 4269–4277, https://doi.org/10.1021/ef900205d.

[56] J. Li, M.C. Paul, K.M. Czajka, Studies of Ignition Behavior of Biomass Particles in a Down-Fire Reactor for Improving Co-firing Performance, Energy Fuels. 30 (2016) 5870–5877, https://doi.org/10.1021/acs.energyfuels.6b01065.

[57] D. Magalhães, F. Kazanç, A. Ferreira, M. Rabaçal, M. Costa, Ignition behavior of Turkish biomass and lignite fuels at low and high heating rates, Fuel 207 (2017) 154–164, https://doi.org/10.1016/j.fuel.2017.06.069.

[58] K.Le Manquais, C. Snape, J. Barker, I. McRobbie, TGA and drop tube furnace investigation of alkali and alkaline earth metal compounds as coal combustion additives, Energy & Fuels 26 (2012) 1531–1539, https://doi.org/10.1021/ef201936g.

[59] O. Senneca, L. Cortese, Kinetics of coal oxy-combustion by means of different experimental techniques, Fuel 102 (2012) 751–759, https://doi.org/10.1016/j.fuel.2012.05.033.

[60] J.J. Murphy, C.R. Shaddix, Combustion kinetics of coal chars in oxygen-enriched environments, Combust. Flame 144 (2006) 710–729, https://doi.org/10.1016/j.combustflame.2005.08.039.

[61] P.A. Bejarano, Y.A. Levendis, Combustion of coal chars in oxygen-enriched atmospheres, Combust. Sci. Technol. 179 (2007) 1569–1587, https://doi.org/10.1080/00102200701239272.

[62] J. Xue, S. Ceylan, J.L. Goldfarb, Synergism among biomass building blocks? Evolved gas and kinetics analysis of starch and cellulose co-pyrolysis, Thermochim. Acta 618 (2015) 36–47, https://doi.org/10.1016/j.tca.2015.09.002.

[63] P. Motiei, M. Pecchi, J.L. Adair, J.L. Goldfarb, J. O'Connor, Pairing combustion experiments and thermogravimetric analysis to uncover timescales controlling cellulose ignition and burnout in a Hencken burner, Combust. Flame 258 (2023) 113092, https://doi.org/10.1016/j.combustflame.2023.113092.

[64] T. Gagić, A. Perva-Uzunalić, Z. Knez, M. Škerget, Hydrothermal Degradation of Cellulose at Temperature from 200 to 300 C, Ind. Eng. Chem. Res. 57 (2018) 6576–6584, https://doi.org/10.1021/acs.iecr.8b00332.

[65] M. Pecchi, Thermogravimetric Analysis in Python, (n.d.). https://pypi.org/project/tga-data-analysis/.

[66] M. Pecchi, J.L. Goldfarb, Open-source Python module to automate GC-MS data analysis developed in the context of bio-oil analyses, RSC Sustain. (2024), https://doi.org/10.1039/D3SU00345K.

[67] Y.A. Levendis, K.R. Estrada, Development of Multi-Color Pyrom-eters to Monitor the Transient Response of Burning Carbonaceous Particles, Effects of Calcium Magnesium Acetate on the" Combustion of Coal-Water Slurries. (n.d.) 26. https://doi.org/10.1063/1.1143586.

[68] J. Riaza, R. Khatami, Y.A. Levendis, L. Álvarez, M.V Gil, C. Pevida, F. Rubiera, J. J. Pis, Single particle ignition and combustion of anthracite, semi-anthracite and bituminous coals in air and simulated oxy-fuel conditions, Combust. Flame 161 (2014) 1096–1108, https://doi.org/10.1016/j.combustflame.2013.10.004.

[69] A. Funke, F. Ziegler, Hydrothermal carbonization of biomass: A summary and discussion of chemical mechanisms for process engineering, Biofuels, Bioprod. Biorefining 4 (2010) 160–177, https://doi.org/10.1002/bbb.198.

[70] J. Chi, L. Zhao, B. Wang, Z. Li, Y. Xiao, Y. Duan, Thermodynamic performance assessment and comparison of IGCC with solid cycling process for CO2 capture at high and medium temperatures, Int. J. Hydrogen. Energy 39 (2014) 6479–6491, https://doi.org/10.1016/j.ijhydene.2014.02.005.

[71] K. Baek, C.-S. Kim, H.-H. Lee, H.-J. Shin, J.-W. Yang, Microbial desulfurization of solubilized coal, Biotechnol. Lett. 24 (2002) 401–405.

[72] Q.Z. G.P. Smith, D.M. Golden, M. Frenklach, N.W. Moriarty, B. Eiteneer, M. Goldenberg, C.T. Bowman, R.K. Hanson, S. Song, W.C. Gardiner Jr., V.V. Lissianski, GRIMech 3.0; (n.d.), (n.d.). http://combustion.berkeley.edu/gri-mech/.

[73] K. Sheng, S. Zhang, J. Liu, E. Shuang, C. Jin, Z. Xu, X. Zhang, Hydrothermal carbonization of cellulose and xylan into hydrochars and application on glucose isomerization, J. Clean. Prod. 237 (2019) 117831, https://doi.org/10.1016/j.jclepro.2019.117831.

[74] X. Du, Ignition and combustion of a dense stream of coal particles, Texas A&M University, 1995.